Thermally induced excitability in injected microcavities with time-delayed feedback

Bachelor thesis

submitted by
Aaron Schwaack

Supervisor:
apl. Prof. Dr. Svetlana Gurevich

Co-Supervisor:
Prof. Dr. Julien Javaloyes

institut für
theoretische physik

Universität Münster

Contents

1 Introduction

Excitability is a fundamental property of many nonlinear dynamical systems encountered in biology, physics, and engineering. An *excitable system* resides near a stable equilibrium but, when perturbed beyond a threshold, produces a large stereotyped excursion in phase space before returning to rest [1]. This character underlies phenomena as diverse as neuronal action potentials [2], chemical oscillations [3], and optical pulse generation [4].

A paradigmatic model for excitability is the FitzHugh–Nagumo (FHN) system, which reduces the Hodgkin–Huxley neuron equations to a slow-fast system that retains the essential phenomenology while remaining analytically tractable [2, 5]:

$$\epsilon \frac{dv}{dt} = v - \frac{v^3}{3} - w + I(t), \tag{1}$$

$$\frac{dw}{dt} = v + a - bw, \tag{2}$$

where v is the fast activator, w the slow recovery variable, $I(t)$ an external stimulus, and $\epsilon \ll 1$ enforces a separation of timescales. Depending on parameter values, the system displays *type I* or *type II* excitability, a classification rooted in the nature of the bifurcation that initiates repetitive neuron firing [1].

Noise-driven excitability has emerged as a key mechanism in systems where stochastic fluctuations trigger excitable responses even without deterministic inputs [6]. Here, phenomena such as *coherence resonance* [7], where an optimal noise amplitude maximizes the regularity of noise-induced oscillations, and *stochastic resonance* [8], where noise enhances the detection of weak periodic signals, have been extensively studied. These effects highlight the constructive role that fluctuations can play in excitable media and have motivated extensive study in neural, chemical, and optical contexts [6].

Excitability is equally relevant in nonlinear optics, where light-matter interactions give rise to rich slow-fast dynamics. In microresonator experiments, the partial absorption of intracavity optical power gradually heats the cavity material, altering its refractive index and thereby shifting the cavity resonance frequency $\omega_c(t)$ over time [4]. Because the effective detuning $\delta(t) = \omega_c(t) - \omega_0$ inherits this thermal drift, a separate dynamical equation must be written for the evolution of the detuning. Because of the slow heating, it evolves on a timescale many orders of magnitude slower than the intracavity electric field dynamics. This separation between fast optical and slow thermal degrees of freedom is precisely the structure that generates excitability. A perturbation can push the system across a threshold, after which it undergoes a large excursion in phase space before the thermal degree of freedom relaxes it back to rest. The resulting pulses are referred to as *thermo-optic pulses* (TOPs). Beyond thermal effects, delayed optical feedback introduces an additional timescale giving rise to multistability, delay-induced switched states, and competition of both timescales, which give rise to new kinds of excitable orbits.

Therefore the thesis investigates the nonlinear dynamics and excitability of the *Kerr–Gires–Tournois interferometer* (KGTI), a microresonator embedding a Kerr nonlinearity, subject to the slow thermo-optic detuning, and coupled to an external feedback cavity driven by continuous-wave injection. The system is described by a delay differential equation (DDE) for the intracavity field coupled to a slow ordinary differential equation (ODE) for the thermal detuning. In the limit of a short external cavity the system reduces to a three-dimensional ODE amenable to a complete slow-fast analysis. When the delay is restored, the infinite-dimensional DDE phase space exhibits additional solution families whose existence, stability, and noise-driven excitability are studied in detail.

The thesis is structured as follows. The mathematical framework of nonlinear dynamical systems is introduced first, covering linear stability analysis for ODEs and DDEs, Floquet theory, and local and global bifurcations, including the canard phenomenon. The KGTI model is then derived and its numerical implementation described. The non-delayed limit is analyzed next: the slow manifold structure, canard explosion, periodic solutions, subthreshold chaos, and noise-induced excitability are characterized in detail. The analysis is subsequently extended to the full delayed system, where τ-periodic switched states, their bifurcation structure, and two distinct excitability regimes including thermo-optic pulses (TOPs) are investigated. Finally, the results are summarized and an outlook for future work is provided.

2 Nonlinear dynamical systems

A *nonlinear system* is defined in contrast to a *linear system*. A function $f : V \to W$ is said to be *linear* if it satisfies the properties of homogeneity and additivity, namely:

$$f(\alpha x + \beta y) = \alpha f(x) + \beta f(y), \tag{3}$$

where $\alpha, \beta \in \mathbb{C}$ and $x, y \in V$. If this condition does not hold, the function is considered to be *nonlinear*. Nonlinear systems are generally more challenging to analyze and solve, as their solutions often cannot be expressed in closed form. Nevertheless, their qualitative behavior can be investigated through analytical tools such as linear stability analysis and bifurcation theory. In contrast to linear systems, nonlinear systems can exhibit a wide range of complex behaviors, including bifurcations, multistability, periodic and quasiperiodic oscillations, and even chaos. These phenomena make nonlinear dynamical systems both rich in structure and difficult to predict. The evolution of a state variable $x(t)$ can generally be described using either differential equations, which are continuous in time, or discrete maps, which evolve at distinct time intervals. Since the systems of interest here are time-continuous, we focus on differential equations. These can be broadly classified into three main categories: ordinary differential equations (ODEs), partial differential equations (PDEs), and delay differential equations (DDEs).

In an ODE, derivatives of the unknown function appear only with respect to a single independent variable, whereas PDEs involve derivatives with respect to multiple independent variables. The *order* of a differential equation is determined by the highest derivative present.

3 Linear stability analysis

The stability of solutions in dynamical systems is a fundamental topic in both ordinary differential equations (ODEs) and delay differential equations (DDEs). This section summarizes the key concepts and methods used to analyze the stability of equilibria and periodic orbits. Consider a general *autonomous* ODE system

$$\dot{x}(t) = f(x(t)), \quad x(t) \in \mathbb{R}^n, \tag{4}$$

where $f : \mathbb{R}^n \to \mathbb{R}^n$ is sufficiently smooth. An equilibrium point x^* satisfies $f(x^*) = 0$.

3.1 Linear stability analysis of ordinary differential equations

A small perturbation $\xi(t)$ around the equilibrium,

$$x(t) = x^* + \xi(t), \quad \|\xi\| \ll 1, \tag{5}$$

evolves according to the linearized system

$$\dot{\xi}(t) = Df(x^*)\xi(t) = A\xi(t) \tag{6}$$

where A is the Jacobian matrix evaluated at x^*. The eigenvalues λ_i of A determine the local stability:

- $\mathrm{Re}(\lambda_i) < 0$ for all i: x^* is locally asymptotically stable.
- $\mathrm{Re}(\lambda_i) > 0$ for any i: x^* is unstable.

3.2 Linear Stability of delay differential equations

This basic idea can also be applied to delay differential equations. Delay differential equations (DDEs) incorporate a time delay in the state [9]:

$$\dot{x}(t) = f\Big(x(t), x(t-\tau_1), \ldots, x(t-\tau_m)\Big), \quad x(t) \in \mathbb{R}^n, \tag{7}$$

where $\tau_i > 0$ are constant delays. Unlike ODEs, the *state at time t* is the entire history function

$$\phi_t(s) = x(t+s), \quad s \in [-\tau_{\max}, 0], \quad \tau_{\max} = \max_i \tau_i. \tag{8}$$

Thus, DDEs are *infinite-dimensional dynamical systems*, since the phase space is the function space $C([-\tau_{\max}, 0], \mathbb{R}^n)$.
Fixed points are defined the same way as in ODEs, but linearization is more intricate.

Let x^* again be an equilibrium. Then the linearization for the DDE yields [9]

$$\dot{\xi}(t) = A_0\xi(t) + \sum_{i=1}^{m} A_i\xi(t-\tau_i), \quad A_i = \frac{\partial f}{\partial x(t-\tau_i)}\Big|_{x^*}. \tag{9}$$

The characteristic equation is obtained by inserting the ansatz $\xi(t) = v\exp\{\lambda t\}$ into Equation 9. This equation is generally transcendental:

$$\det\left(\lambda I - A_0 - \sum_{i=1}^{m} A_i e^{-\lambda\tau_i}\right) = 0, \tag{10}$$

leading to infinitely many eigenvalues. Stability is then determined by the eigenvalue with the largest real part and the same criteria for the ODE system can be applied.

4 Stability of periodic solutions

In the previous section stability of fixed points were investigated. However, in many systems periodic solutions exists. For these solutions a different tool for analyzing stability must be employed.
Therefore, consider a system of differential equations with a periodic solution:

$$\dot{x} = f(x, t), \quad x \in \mathbb{R}^n, \quad f(x, t + T) = f(x, t), \tag{11}$$

where T is the period. Let $x_p(t)$ be a T-periodic solution. To determine the stability of this periodic orbit, we analyze the corresponding fixed point x^* of the associated Poincaré map [10]. Let S denote a transverse section to the flow that intersects the closed orbit. Then, the Poincaré map

$$P : S \to S$$

is defined such that $P(x_0)$ is the next intersection of the trajectory starting from $x_0 \in S$ with the section S. Thus, the periodic orbit corresponds to a fixed point x^* satisfying

$$P(x^*) = x^*$$

meaning that the orbit reconnects to itself. Now, consider a small perturbation ξ_0 such that $x^* + \xi_0 \in S$. After one return to S, the map yields

$$\begin{aligned} x^* + \xi_1 &= P(x^* + \xi_0) \\ &= P(x^*) + [DP(x^*)]\xi_0 + \mathcal{O}(\|\xi_0\|^2) \\ &= x^* + [DP(x^*)]\xi_0 + \mathcal{O}(\|\xi_0\|^2), \end{aligned} \tag{12}$$

where $DP(x^*)$ is the *linearized Poincaré map* (Jacobian matrix) evaluated at the fixed point x^*. Neglecting higher-order terms, we obtain the linear relation

$$\xi_1 = [DP(x^*)]\xi_0. \tag{13}$$

The matrix $DP(x^*)$ has $(n-1)$ eigenvalues for a n-dimensional system, denoted by μ_j, called the *characteristic* or *Floquet multipliers* of the periodic orbit. The linear stability of the orbit is determined by the magnitudes of these multipliers:

$$|\mu_j| < 1 \quad \text{for all } j = 1, \dots, n-1$$

implies that the periodic orbit is *linearly stable*, while if $|\mu_j| > 1$ for any j, the orbit is *unstable*.
To understand this, assume the eigenvectors $\{\mathbf{e_j}\}$ of $DP(x^*)$ form a basis of the

tangent space to S. Then, an arbitrary perturbation can be expressed as

$$\xi_{\mathbf{0}} = \sum_{j=1}^{n-1} \mu_j \mathbf{e_j},$$

After k iterations, we obtain

$$\xi_{\mathbf{k}} = \sum_{j=1}^{n-1} \mu_j^k \xi_j \mathbf{e_j}. \tag{14}$$

Here the perturbation $\xi \in \mathbb{R}^{n-1}$ is written in bold to distinguish the vector from its components. It then follows from the mapping that the stability criteria are:

- $|\mu_i| < 1$ for all i: the periodic orbit is **asymptotically stable**.
- $|\mu_i| > 1$ for some i: the periodic orbit is **unstable**.

Finally, note that there is always one *trivial multiplier* $\mu = 1$ associated with perturbations tangent to the periodic orbit, corresponding to time translation along the orbit since the section S transverse to the orbit is $n-1$ dimensional [10]. For DDEs the characteristic equation has infinitely many roots and the largest Floquet multiplier determines the stability. In practice, computing intersections is time-consuming, therefore tools like *dde-biftool* compute the monodromy matrix, which essentially maps perturbations over one period like

$$\xi(T) = M\xi(0), \tag{15}$$

is obtained solving the system via a collocation method[9]. In the DDE case the points $\xi(T)$ and $\xi(0)$ involve the entire history function, so that M actually an operator that can only be represented by a matrix if the history function is discretized.

5 Local bifurcations

A *bifurcation* occurs when a small change in a system parameter, called the control parameter, causes a qualitative change in the system's behavior [10]. The results of a bifurcation analysis are often summarized in a bifurcation diagram, where the parameter is plotted against the location of fixed points. The resulting lines of fixed points are referred to as *branches*, and at a bifurcation point the stability of a branch changes, typically when the real part of an eigenvalue crosses the imaginary axis. Additional branches may also emerge from a bifurcation point, and the precise behavior there defines the type of bifurcation, which can be described using a *normal form*. Systems exhibiting the same bifurcation type are locally topologically equivalent to its normal form. In the following, several bifurcation types relevant for this thesis are presented.

5.1 Period doubling bifurcation

Period doubling occurs when a Floquet multiplier crosses -1 on the real axis. At this point, a stable period-T orbit loses stability and a new stable period-$2T$ orbit emerges, since the perturbations now have two attracting points in the $(\xi(t), \xi(t+T)$-space. Formally, if M has a multiplier $\mu = -1$, the system exhibits

$$x(t + 2T) \approx x(t),$$

indicating a doubling of the orbit's period. This can also be seen in Figure 2

5.2 Hopf bifurcation

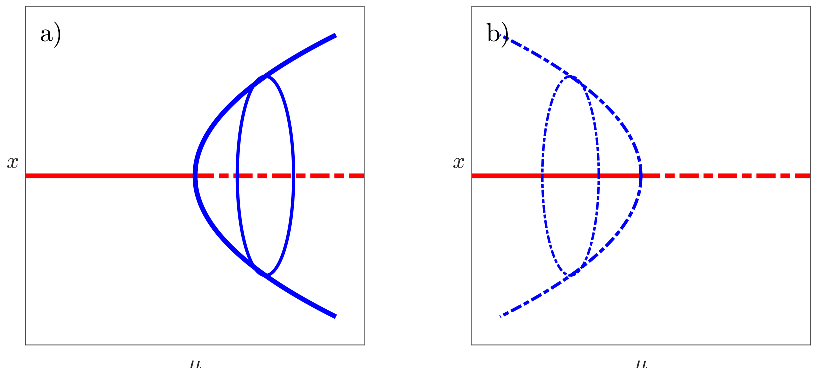

Figure 1: a) Supercritical Hopf bifurcation: A stable fixed point (red) loses stability and creates a stable limit cycle (blue). b) Subcritical Hopf bifurcation: A stable fixed point(red) collides with an unstable limit cycle(blue) and loses stability.

Another important bifurcation that occurs on fixed point branches is the *Hopf bifurcation* (also Andronov-Hopf), where a pair of complex conjugate eigenvalues crosses the imaginary axis and the fixed point loses stability [10]. This is the reason why

Hopf bifurcations can only occur in two- or higher-dimensional systems. Two cases of a Hopf bifurcation must be distinguished. in the supercritical bifurcation, a stable fixed point becomes unstable and a stable limit cylce is born. In case of the subcritical Hopf bifurcation a stable fixed point collides with an unstable limit cycle and becomes unstable in the process. The normal form of the supercritical Hopf bifurcation in polar coordinates is

$$\begin{aligned} \dot{r} &= \mu r - r^3 \\ \dot{\theta} &= \omega + br \end{aligned} \tag{16}$$

where r controls the stability of the fixed point and ω the frequency of the local oscillations. In Cartesian coordinates the system becomes

$$\begin{aligned} \dot{x} &= rx - \omega y + \text{cubic terms} \\ \dot{y} &= \omega x - ry + \text{cubic terms} \end{aligned} \tag{17}$$

The Jacobian at the origin (fixed point) is

$$Df(0) = \begin{pmatrix} \mu & -\omega \\ \omega & \mu \end{pmatrix} \tag{18}$$

with eigenvalues

$$\lambda = \mu \pm i\omega. \tag{19}$$

Thus, for $\mu = 0$ a Hopf bifurcation occurs, so there is now a outward spiral away from the fixed point instead of an inward spiral.

5.3 Torus bifurcation

A torus bifurcation arises when a pair of complex-conjugate Floquet multipliers cross the unit circle $|\mu| = 1$ [10]. This means that an already periodic orbit with frequency ω_1 becomes modulated with an additional frequency ω_2, thus moving on a 2-torus. If the ratio $\frac{\omega_1}{\omega_2}$ ist is rational the orbits close on the torus, if the ratio is irrational the orbit densely cover the torus, and does not intersect itself. The behavior of the Floquet multipliers is displayed in Figure 2

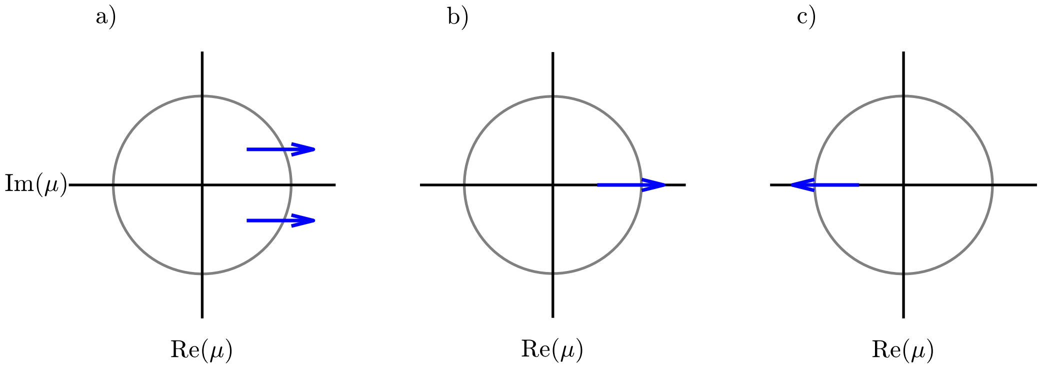

Figure 2: bifurcation behavior of Floquet multipliers for a) a Torus (T) or Hopf (H) bifurcation, b) a fold bifurcation and a c) period-doubling bifurcation (PD). The arrows indicate the movement of the floquet multipliers from the stable to the unstable regime along a solution branch leaving the unit circle (gray). The axes denote the imaginary and real part of the multipliers respectively.

5.4 Saddle-node bifurcation

In a *saddle node bifurcation* (alternatively *fold bifurcation*) two fixed points come into existence, where one is stable the other one unstable. The normal form [10]

$$\dot{x} = r + x^2 \tag{20}$$

has r as a control parameter. Only for $r \geq 0$ the fixed points $x^* = \pm\sqrt{|r|}$ exist. Since the Jacobian simply is

$$Df(x^*) = 2x^*, \tag{21}$$

the fixed point $x^* = -\sqrt{|r|}$ is stable and $x^* = +\sqrt{|r|}$ is locally unstable. For $x^* = 0$ the fixed point is metastable. The resulting bifurcation diagram is shown in Figure 3.

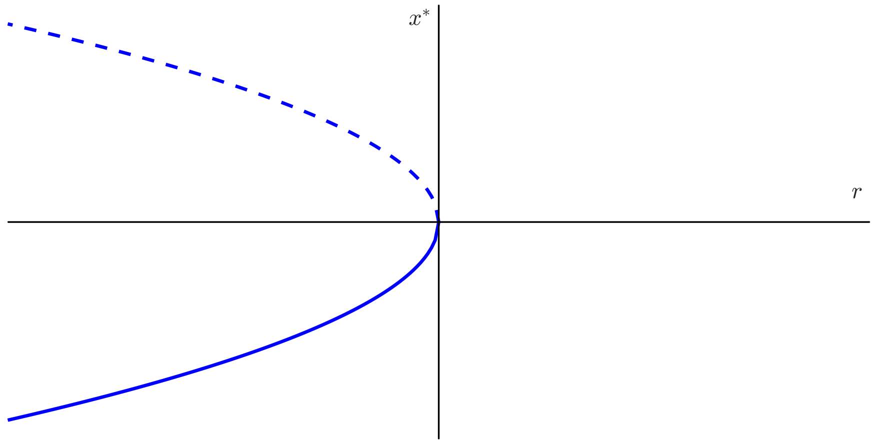

Figure 3: Bifurcation diagram of a fold bifurcation. Two fixed points $\pm\sqrt{|r|}$ exist for $r < 0$. The unstable fixed point is indicated by a dashed line and the stable fixed point is solid.

For periodic orbits, a *fold* bifurcation occurs when two limit cycles are created or collide and annihilate each other. Along a stable branch, this corresponds to a real Floquet multiplier crossing $\mu = 1$ at the bifurcation point, so that the orbit loses or gains stability precisely when the two cycles coalesce or disappear.

6 Excitability

Excitability is a dynamical regime in which a system at rest is capable of producing a large, stereotyped response when perturbed sufficiently. Unlike regular oscillations, in which e.g. pulses fire repetitively, an excitable system fires once per suprathreshold perturbation before returning to its equilibrium. Unlike a stable node, it does not relax immediately but first executes a long excursion through phase space [1]. Three properties are considered hallmarks of excitability [1]:

1. **Threshold behaviour.** There exists a sharp boundary in phase space separating sub- and suprathreshold perturbations. Stimuli below threshold evoke only small local relaxation. Stimuli above threshold trigger a qualitatively distinct, large-amplitude response.

2. **Stereotypy.** The suprathreshold response is essentially independent of the stimulus strength: once the threshold is crossed, the excursion follows a trajectory largely determined by the system's intrinsic dynamics rather than by the details of the perturbation.

3. **Refractoriness.** Following a suprathreshold excursion the system passes through a refractory period during which it cannot be re-excited, before eventually recovering its resting excitability.

These properties emerge naturally from slow-fast structure, where fast variable drives the large excursion while a slow recovery variable enforces the return to rest and the refractory period.

6.1 The FitzHugh-Nagumo model

A prominent biological example of an excitable system is the neuron. Neurons rest at a negative membrane potential and, upon receiving a sufficiently large synaptic input, generate an *action potential*, which consists of a rapid depolarization of the membrane followed by a slower recovery phase, after which the resting potential is restored [1]. This behaviour is described in quantitative detail by the Hodgkin-Huxley (HH) model [11]. However, the essential geometric structure underlying excitability is already apparent in the reduced two-dimensional FitzHugh-Nagumo (FHN) system: [2, 5]:

$$\epsilon \frac{dv}{dt} = v - \frac{v^3}{3} - w + I, \tag{22}$$

$$\frac{dw}{dt} = v + a - bw. \tag{23}$$

Here v is the fast activator representing to membrane voltage, w the slow recovery variable representing the ion channels, I a constant applied injection current, and $\epsilon \ll 1$ the small parameter that enforces the separation of timescales. The parameters a and b control the position of the resting state and the rate of recovery respectively.

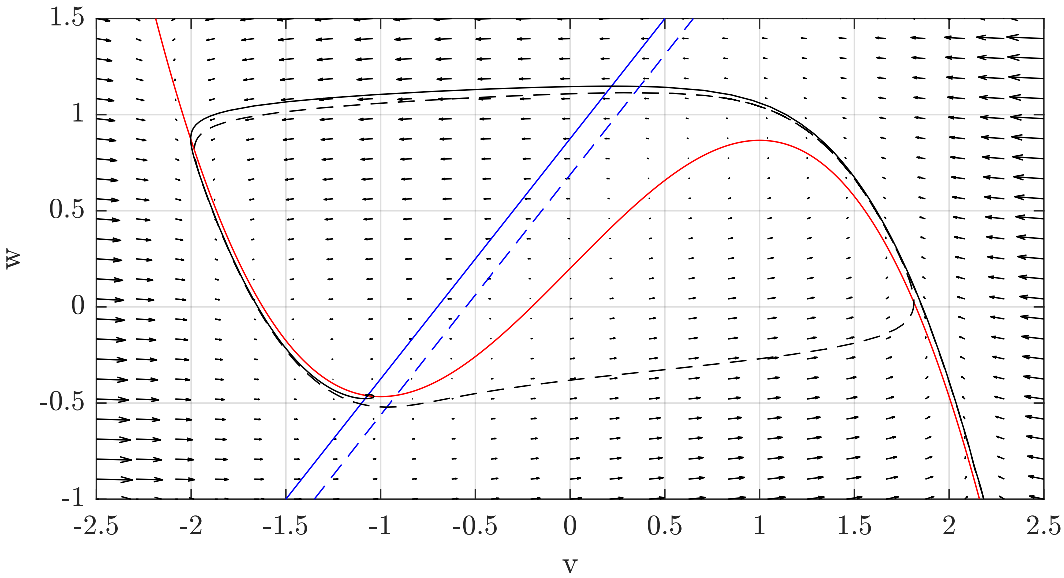

Figure 4: Phase portrait of the FitzHugh-Nagumo model including the flow, the nullclines and 2 different orbits with $a = 0.7\,(0.55)$, $b = 0.8$, $\tau = 12.5$ and $I = 0.2$, the solid lines represents a stable fixed point solution and the dashed line represents a relaxation oscillation similar to pulse.

The dynamics are most transparently understood through the *nullclines*: the curves in the (v, w) phase plane on which $\dot{v} = 0$ and $\dot{w} = 0$ respectively. The v-nullcline, $w = v - v^3/3 + I$, is a cubic with a local maximum and minimum. The w-nullcline, $w = (v + a)/b$, is a line of small positive slope. Their behavior can be seen in Figure 4. In the excitable regime these curves intersect at a single stable fixed point located on the left branch of the cubic.

A suprathreshold perturbation displaces v beyond the local maximum of the cubic, after which the fast dynamics carry the trajectory rapidly to the right branch of the v-nullcline. There, w grows slowly until it exceeds the right knee of the cubic nullcline of v, whereupon the trajectory jumps back to the left branch and w decays slowly back to the fixed point. The result is a single large pulse in v followed by a refractory recovery phase set by the slow variable w. The pulses therefore resemble the stable relaxation oscillations when the fixed point becomes unstable (cf. dashed orbit in Figure 4. In thermo-optical systems such as the KGTI with thermal effects the characteristic noise spike analogous to the neuron firing is referred to as a thermo-optical pulse (TOP).

6.2 Type I and Type II excitability

Not all excitable systems are equivalent. Hodgkin [12] originally distinguished two classes of nerve membrane based on their current to frequency relationship, a classification that can also be applied to non-neural systems [1].

Type I excitability arises when the transition from rest to repetitive firing occurs via a saddle-node bifurcation. At the threshold, a stable and a saddle point equilibrium collide and annihilate on a limit cycle, and the period of that cycle diverges as the bifurcation point is approached. Consequently, Type I neurons can fire at arbitrarily low frequencies, and their firing rate grows continuously from zero [13].

Type II excitability arises instead when repetitive firing is born in a *Hopf bifurcation*, so the limit cycle appears at a finite, non-zero frequency. Type II systems therefore exhibit a discontinuous jump in firing rate at threshold and cannot sustain arbitrarily slow oscillations. The FHN system (22)–(23) generically displays Type II behavior, since the destabilization of the fixed point as I increases proceeds through a Hopf bifurcation.

The distinction between Type I and Type II behaviour has direct consequences for synchronization, phase-locking, and sensitivity to noise, and it extends beyond neuroscience. Optical and chemical excitable systems have likewise been assigned to one class or the other based on the bifurcation structure near their resting states [6].

6.3 Noise-induced excitability

In many physical and biological settings, excitable systems are subject to stochastic fluctuations. Even in the absence of any deterministic suprathreshold stimulus, noise can repeatedly drive the system across threshold, producing a trace of *noise-induced pulses* [6].

A property of some systems with noise-driven excitability is *coherence resonance*, described numerically in the FHN model by Pikovsky and Kurths [7]. As the noise amplitude is increased from near zero, the regularity of the noise-induced pulse train first increases and then decreases, passing through a maximum at an intermediate, optimal noise level.

6.4 Canard phenomenon

Type II excitability is often accompanied by a bifurcation scenario where the amplitude of the small Hopf cycle rapidly amplifies with variation of the parameter. To understand this Canard phenomenon, we consider a slow-fast dynamical system of the form

$$\varepsilon \dot{x} = f(x, y, \lambda), \qquad \dot{y} = g(x, y, \lambda), \tag{24}$$

where $0 < \varepsilon \ll 1$ is the singular perturbation parameter, $x \in \mathbb{R}^n$ denotes the fast variable, $y \in \mathbb{R}^m$ the slow variable, and λ a system parameter. The dynamics of such systems are governed by the interplay between the fast and slow timescales, and are naturally analyzed via the critical manifold which serves as the phase space skeleton in the singular limit $\varepsilon = 0$. On normally hyperbolic portions of the critical manifold, there exists a nearby slow manifold, along which trajectories evolve slowly [14].

The critical manifold generically contains *fold points*, where normal hyperbolicity fails and the manifold folds over itself. At such points, trajectories are typically forced to leave the slow manifold and undergo a rapid excursion along the fast direction [14].

The canard phenomenon is closely connected to Hopf bifurcation since they occur near a Hopf point in slow–fast systems with the small parameter ϵ. As a parameter λ passes through a critical value λ_0, a Hopf bifurcation typically gives rise to a family of small-amplitude periodic orbits. In a narrow parameter regime that is exponentially small in ϵ, these periodic orbits undergo a dramatic transition. Solutions begin to follow segments of both attracting and repelling slow manifolds, leading to an abrupt change from small-amplitude oscillations near equilibrium to large-amplitude relaxation oscillations. This phenomenon, known as the *canard explosion*, has been rigorously analyzed using geometric desingularization (blow-up) techniques [14]. A closer examination with application to the thermal KGTI system is given in section 8.

7 Modeling of the thermal Kerr-Gires-Tournois Interferometer (KGTI) and numerical methods

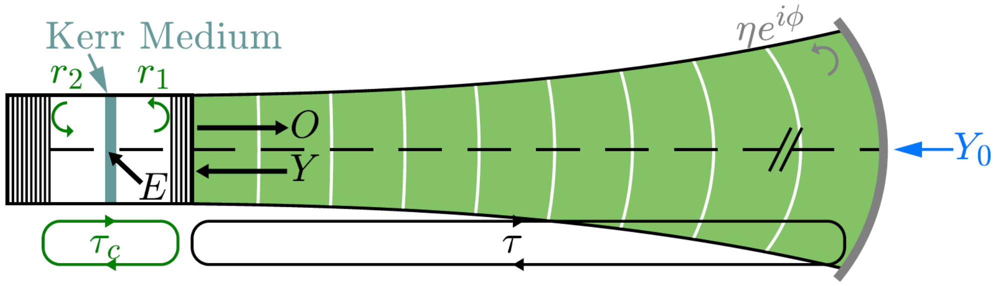

Figure 5: Scheme of the Kerr Gires-Tourois interferometer (KGTI) [15] It contains a large external cavity with a field Y which has a round trip time of τ and an injection Y_0. Inside the microcavity there is the field E at the Kerr medium.

We consider a monomode microcavity of length L, bounded by two Bragg mirrors located at $z = 0$ and $z = L$, with reflection coefficients r_1 and r_2 for the top and bottom mirrors, respectively. The intracavity field is split into forward (+) and backward (−) propagating waves, and a thin Kerr nonlinear slice is placed at a field anti-node $z = l$ to maximize nonlinear interactions. The microcavity is coupled to an external cavity of length much larger than the microcavity, with round-trip time τ, closed by a feedback mirror with reflectivity η and phase ϕ. The system is driven by a continuous-wave (CW) injection of amplitude Y_0 and frequency ω_0. The thermal effects are included by a equation for the thermal detuning δ which describes the frequency shift that results from the heating.
Following the derivation in [16] and [4], and including thermal effects and propagation losses, the dynamics of the intracavity field $E(t)$, the nonlinear detuning $\delta(t)$, and the external cavity field $Y(t)$ are described by the following equations:

$$\begin{aligned} \dot{E}(t) &= h\Big[-1 + i\left(|E(t)|^2 - \delta(t)\right)\Big]E(t) + hY(t), \\ \dot{\delta}(t) &= \gamma\left[\delta_0 - \delta(t) - \mu_\alpha |E(t)|^2\right], \\ Y(t) &= \eta e^{i\phi}\left[E(t-\tau) - Y(t-\tau)\right] + \sqrt{1-\eta^2}Y_0. \end{aligned} \tag{25}$$

Here, the variables and parameters are defined as follows [4]:

- $E(t)$: slowly varying envelope of the intracavity electric field.
- $Y(t)$: slowly varying envelope of the field in the external cavity.
- $O(t)$: output field, defined by the input-output relation $O = E - Y$.
- $\delta(t)$: detuning of the microcavity resonance relative to the injected field, including nonlinear and thermal contributions.

- h: coupling efficiency of the injected field into the cavity, depending on r_1 and r_2.
- γ: thermalization rate of the cavity, representing the slow dynamics of the thermal response.
- μ_α: thermal nonlinearity coefficient, proportional to thermo-optic effects and thermal resistance of the medium.
- δ_0: intrinsic detuning of the cavity in the absence of thermal effects.
- τ: round-trip time of the external cavity.
- η: amplitude reflectivity of the feedback mirror in the external cavity.
- ϕ: total round-trip phase of the external cavity including mirror phase and propagation.
- Y_0: amplitude of the continuous-wave input field.

The derivation of the system proceeds as follows:

1. The intracavity field is described as a sum of forward and backward propagating waves, split across the Kerr medium at a field anti-node. Also, only transverse modes are considered. Finally, the field is expanded around the carrier frequency of the CW injection ω_0.
2. Reflection and transmission at the Bragg mirrors lead to the coupling factor $h = \frac{(1-|r_1|)(1+|r_2|)}{1-|r_1 r_2|}$, which characterizes the effective injection into the microcavity.
3. The external cavity is coupled back to the microcavity field after one round-trip, resulting in the delayed input term for Y.
4. The thermal detuning $\delta(t) = \omega_c(t) - \omega_0$ equation is obtained by expressing the cavity resonance shift as a consequence of temperature variations, using a temperature balance equation that includes both relaxation toward an equilibrium temperature and heating from absorbed optical power. Relating the refractive index of the Kerr element to the temperature equation and cavity resonance frequency ω_c which is assumed to be in the vicinity of the CW frequency ω_0, the differential equation for the detuning is obtained.

In practice, this system exhibits both fast Kerr-induced dynamics in the intracavity field $E(t)$ and slow thermal dynamics in the detuning $\delta(t)$, with the delay τ introducing additional complexity including feedback mechanisms and delay-induced oscillations.

7.1 Numerical integration of ODEs and DDEs

As stated in section 2, in many cases it is not possible to find a closed analytical form of a nonlinear dynamical system. This is the reason why numerical methods are employed in order to approximate the solution. For this, it is necessary to discretize the time and for PDEs the spatial variables. A simple method for DDEs is *Euler's method* [10], which can be used for DDEs of the form

$$\dot{x}(t) = f(x(t), x(t-\tau_1), \dots, x(t-\tau_N), t) \tag{26}$$

with N delays. Then then time step Δt is chosen such that for all τ_i the fraction $m_i = \frac{\tau_i}{\Delta t}$ is always a natural number. In contrast to an ODE the initial condition consists of a discrete function $x_0(s)$ over the interval $s \in \{-\max_i(\tau_i), -\max_i(\tau_i) + \Delta t, \dots, -\Delta t, 0\}$. *Euler's method* is based on the Taylor expansion of $x(t_n + \Delta t) = x_{n+1}$ which yields the iteration formula

$$\begin{aligned} x_{n+1} &= x_n + \dot{x}\big|_{t_n} \cdot \Delta t + \mathcal{O}((\Delta t)^2) \\ &= x_n + \Delta t \cdot f(x_n, x_{n-m_1}, \dots, x_{n-m_N}, t_n) + \mathcal{O}((\Delta t)^2) \end{aligned} \tag{27}$$

For computation, the scheme is truncated after $\mathcal{O}(\Delta t)$, so that the local error is $\mathcal{O}((\Delta t)^2)$, while the global truncation error is $\mathcal{O}(\Delta t)$. So, the method may sometimes not be accurate enough, since the derivative over the full interval $[t_n, t_n + \Delta t]$ is assumed to be constant. Nonetheless, an implicit or more precicesly a semi-implicit Euler scheme is implemented[16]. Starting with the KGTI equations with thermal detuning which are given by

$$\begin{aligned} \dot{E} &= h\Big[-1 + i\left(|E|^2 - \delta\right)\Big]E + hY, \\ Y &= \eta e^{i\phi}(E_\tau - Y_\tau) + \sqrt{1-\eta^2}Y_0, \\ \dot{\delta} &= \gamma\Big(\delta_0 - \delta - \mu_\alpha |E|^2\Big). \end{aligned} \tag{28}$$

where $E(t)$ and $Y(t)$ are complex fields, δ is the thermal detuning, τ is the only delay and other variables are system parameters. As a shorthand notation $E_\tau = E(t-\tau)$ and $Y_\tau = Y(t-\tau)$ is introduced. For the numerical integration, let $E_n = E(t_n)$ and define

$$L_n = -1 + i(|E_n|^2 - \delta). \tag{29}$$

The standard explicit Euler method for this system would be

$$E_{n+1} = E_n + \Delta t \left(L_n E_n + hY_n\right), \tag{30}$$

The semi-implicit Euler scheme introduces E_{n+1} on both sides to improve accuracy by averaging E and Y:

$$E_{n+1} = E_n + \Delta t \left[L_n \frac{E_{n+1} + E_n}{2} + h \frac{Y_{n+1} + Y_n}{2} \right]. \tag{31}$$

Rewriting this semi-implicitly gives

$$E_{n+1} = \left(1 - \frac{\Delta t}{2} L_n\right)^{-1} \left[\left(1 + \frac{\Delta t}{2} L_n\right) E_n + \frac{\Delta t}{2} h(Y_{n+1} + Y_n) \right]. \tag{32}$$

The evolution of Y_{n+1} of the algebraic equation is given by

$$Y_{n+1} = \eta e^{i\phi} \left(E_{n-N+1} - Y_{n-N+1}\right) + \sqrt{1-\eta^2} Y_0, \tag{33}$$

where $N = \tau/\Delta t$ is the number of timesteps corresponding to the delay. The equation for δ is just computed by the explicit scheme because it has much slower dynamics. The initial condition is an $N \times 5$ array representing one delay interval of the real and imaginary parts of E and Y and δ respectively. In case of the non-delayed ODE system, the equation for Y becomes an alegebraic equation, that can uniquely be solved for Y.

7.2 Numerical path continuation

Numerical continuation is a powerful tool for analyzing dynamical systems, as it enables the exploration of system behavior across parameter space and allows tracking of both stable and unstable solution branches. In addition, it facilitates the detection of bifurcations, providing a means to identify and follow the emergence of new solution branches.

For the presented method [17], assume a general ODE system with a parameter μ such that $f(x^*, \mu) = 0$. If the Jacobian is non-singular any regular solution (x^*, μ) lies on a continuous branch. First we need Newton's method, which is a root finding algorithm that solves $f(x) = 0$. In one dimension the iteration formula states

$$x^{(i+1)} = x^{(i)} + \frac{f(x^{(i)})}{f'(x^{(i)})} \tag{34}$$

which is obtained from the Taylor expansion of $f(x)$. Similiarly, in n dimensions the expansion gives us

$$Df(x^{(i)})\Delta x = -f(x^{(i)}) \tag{35}$$

where $x^{(i+1)} - x^{(i)} = \Delta x$. In both cases the process starts from an initial guess $x^{(0)}$ which can be obtained by direct numerical simulations. Since the goal is to follow the solution branch (x, μ) the initial guess for the next parameter value μ_{j+1}. Hence, the tangent $\frac{\partial x}{\partial \mu}$ is needed, which can simply be obtained by differentiating

$f(x(\mu),\mu)|_{x_j,\mu_j} = 0$ with respect to μ. Then by the chain rule

$$\frac{\partial f}{\partial x}\frac{\partial x}{\partial \mu}\bigg|_{x_j,\mu_j} + \frac{\partial f}{\partial \mu}\bigg|_{x_j,\mu_j} = 0 \tag{36}$$

the tangent vector can be determined by solving this system of linear equations. Then, the first linear prediction for x_{j+1} is

$$x_{j+1} = x_j + \frac{\partial x}{\partial \mu}\bigg|_{x_j,\mu_j} \Delta\mu \tag{37}$$

In the next step, again the Newton correction from Equation 35 is applied to this prediction. This method works perfectly fine until the branch reaches a fold or saddle-node bifurcation at $\mu = \mu_f$. Now, for $\mu < \mu_f$ two solutions exist but none for $\mu > \mu_f$. This problem can be resolved by the *pseudo-arclength method*.
To avoid the previous problem, a parameter that is monotonous along the branch is needed. This is fulfilled by the arclength along the branch, which fulfills

$$\begin{aligned}(\Delta s)^2 &= |\Delta x|^2 + (\Delta\mu)^2 \\ &\approx \Delta x \frac{\partial x}{\partial s}\Delta s + \Delta\mu\frac{\partial \mu}{\partial s}\Delta s\end{aligned} \tag{38}$$

This condition can now be rewritten into the function

$$p(x,\mu,s) = \Delta x\frac{\partial x}{\partial s} + \Delta\mu\frac{\partial\mu}{\partial s} - \Delta s = 0 \tag{39}$$

If the parameter μ is treated as a new dependent variable, the extended system can be expressed as

$$E(y,s) = \begin{pmatrix} F(y,s) \\ p(y,s)\end{pmatrix} = 0 \tag{40}$$

with $y = (x,\mu)$ as the dependent variable. Equivivalently to the previous method, the tangent $\frac{\partial y}{\partial s}$ is computed for the predictor step and then Newton's method is applied up to the desired accuracy.

7.3 Numerical continuation of periodic orbits

The previous section introduced a path continuation method for fixed points, but extending it to periodic orbits requires additional refinements. First, the goal is to find solutions in discretized time that fulfill $x(t) = x(t+T)$. Hence, tools such as *dde-biftool* employ a collocation-based approach for computing periodic solutions and their stability. To treat the period as an unknown, a time rescaling $t \mapsto t/T$ is introduced. The system then takes the form [9]

$$\dot{x}(t) = Tf(x(t), x(t-\tau)), \tag{41}$$

so that the rescaled periodic orbit has a period of 1. For the numerical implementation, the interval $[0, 1]$ is subdivided into L mesh intervals in order to resolve fast structures more efficiently. The system is then evaluated at the collocation points

$$c_{i,j} = t_i + c_j(t_{i+1} - t_i), \tag{42}$$

where $c_j \in (0, 1)$ and t_i are the interval boundary values. Then for d points per interval and L intervals there are $n(Ld + 1)$ values $x_{ij} = x(c_{ij})$. $\dot{x}_{ij}$ can then be computed by a (e.g. Lagrange interpolation) polynomial having x_{ij} as coefficients, so there are nLd equations of type

$$\dot{x}_{ij} - Tf(x_{ij}, x(c_{ij} - \tau/T)) = 0, \tag{43}$$

where the value of $x(c_{ij} - \tau/T)$ is computed using the polynomial representation. Another n equations are obtained by enforcing periodicity and the last equation is a phase condition restricting the time shift invariance of periodic orbits, so that the number of variables and equations match, which results in a nonlinear system of the form [9]

$$F(\mathbf{x}, T) = 0, \tag{44}$$

where $\mathbf{x}$ collects all collocation coefficients $x_{i,j} \in \mathbb{R}^n$. Given an initial guess obtained, e.g. via numerical time integration, the resulting nonlinear system is solved using Newton's method.

Once a periodic solution $(\mathbf{x}^*, T^*)$ has been computed, continuation in system parameters is performed using a pseudo-arclength continuation method. Instead of recomputing full Jacobians to obtain a tangent vector at each step, *dde-biftool* employs a secant approximation based on the normalized difference of the two previously computed solutions [9].

The continuation step is then corrected by solving the same bordered Newton system described in Equation 40, accompanied by a pseudo-arclength condition enforcing orthogonality of the correction to the secant direction similar to Equation 39. Moreover, if Newton corrections fail or accuracy is insufficient, intermediate points are inserted between previously computed solutions, effectively refining the step size and improving the secant direction for subsequent predictions. If a prediction is correct the step size is in turn increased by a certain factor [9].

In *dde-biftool*, the monodromy operator (cf. section 4) is not computed explicitly. Instead, a discretized approximation is constructed using the same collocation framework as for the periodic orbit. This leads to a finite-dimensional eigenvalue problem whose spectrum approximates the Floquet multipliers. The resulting multipliers are then used as a direct indicator of local stability along the continuation branch [9].

8 Dynamics of the non-delayed system

In the non-delayed case, the excursion time τ of the originally large cavity is set to 0, which is justified for a small external cavity. In this limiting case, the system dynamics reduce to

$$\begin{aligned} \dot{E}(t) &= \Big[-1 + i(|E(t)|^2 - \delta(t))\Big]E(t) + h\,Y(t), \\ Y(t) &= \eta\, e^{i\phi}\Big[E(t) - Y(t)\Big] + \sqrt{1-\eta^2}\,Y_0, \\ \dot{\delta}(t) &= \gamma\Big(\delta_0 - \delta(t) - \mu_\alpha |E(t)|^2\Big). \end{aligned} \tag{45}$$

Thus, the second equation is an algebraic equation for Y, yielding a three-dimensional ODE. Following the standard linear stability analysis, the Jacobian of the system has to be calculated. The real part of the E-field is denoted by E_R, and the imaginary part by E_I. In these coordinates, the Jacobian is

$$Df(E_R, E_I, \delta) = \begin{pmatrix} -2E_RE_I + z_R - 1 & 3E_I^2 - E_R^2 + \delta - z_I & E_I \\ 3E_R^2 + E_I^2 - \delta + z_I & 2E_IE_R + z_R - 1 & -E_R \\ -2\gamma\mu_\alpha E_R & -2\gamma\mu_\alpha E_I & -\gamma \end{pmatrix}, \tag{46}$$

where the complex parameter

$$z = \frac{h\eta e^{i\varphi}}{1 + \eta e^{i\varphi}} \tag{47}$$

is introduced to simplify the expressions. Since

$$\nabla F(E_R, E_I, \delta) = \mathrm{Tr}\big(Df(E_R, E_I, \delta)\big) = 2(z_R - 1) - \gamma < 0,$$

as

$$\max_{\varphi} \mathrm{Re}\left(\frac{h\eta e^{i\varphi}}{1 + \eta e^{i\varphi}}\right) < 1$$

for $h = 2$ and $\eta = 0.7$, we observe that phase-space volumes always decrease, and we end up with solutions in a limiting set.
For small thermal effects, $\gamma \ll 1$, so we can effectively write the system as a slow-fast system, where γ acts as a small-scale parameter. In this way, the original dynamics

$$\begin{aligned} \dot{E} &= f(E, \delta, \gamma), \\ \dot{\delta} &= \gamma\, g(E, \delta, \gamma) \end{aligned} \tag{48}$$

can, in the singular limit $\gamma \to 0$, be reduced to

$$\begin{aligned} \dot{E} &= f(E, \delta, 0), \\ \dot{\delta} &= 0, \end{aligned} \tag{49}$$

where δ is treated as a quasi-static slow variable. This reduction allows us to analyze the fast dynamics of E independently of the slow evolution of δ. To study local stability, we consider small perturbations δE around the critical manifold defined by the nullcline for E,

$$h(E) \quad \text{such that} \quad f(E, h(E)) = 0. \tag{50}$$

This can be derived by introducing the slow time $t_s = \gamma t$, so that the equation for the fast variable reads

$$\gamma \frac{dE}{dt_s} = f(E, \delta, \gamma). \tag{51}$$

Taking the limit $\gamma \to 0$ then yields $f(E, \delta, 0) = 0$.
In order to obtain an analytical expression for the manifold, we can write the condition as $M \cdot x = b$, where x consists of the imaginary and real parts of E, and b is a constant vector depending only on parameters:

$$Mx = \begin{pmatrix} M_{11} & M_{12} \\ -M_{12} & M_{11} \end{pmatrix} \begin{pmatrix} E_R \\ E_I \end{pmatrix} = \begin{pmatrix} (z_R - h)\sqrt{1-\eta^2} Y_0 \\ z_I \sqrt{1-\eta^2} Y_0 \end{pmatrix} = b. \tag{52}$$

Solving for E_R and E_I gives

$$\begin{aligned} E_R &= \frac{(-z_R + h)\sqrt{1-\eta^2} Y_0 M_{11} + z_I \sqrt{1-\eta^2} Y_0 M_{12}}{M_{11}^2 + M_{12}^2}, \\ E_I &= \frac{(-z_R + h)\sqrt{1-\eta^2} Y_0 M_{12} - z_I \sqrt{1-\eta^2} Y_0 M_{11}}{M_{11}^2 + M_{12}^2}. \end{aligned} \tag{53}$$

The matrix elements are

$$M_{11} = z_R - 1, \qquad M_{12} = \delta - |E|^2 + z_I. \tag{54}$$

Taking the absolute value $|E|^2$ of Equation 53 and performing further algebraic manipulations yields the quadratic equation

$$\delta^2 + c_1(|E|^2)\,\delta + c_2(|E|^2) = 0. \tag{55}$$

The coefficients c_1 and c_2 are functions of $|E|^2$:

$$\begin{aligned} c_1 &= (z_R - 1)^2 + z_I^2 + (|E|^2)^2 + 2z_I|E|^2 - \frac{A}{|E|^2}, \\ c_2 &= -2|E|^2 - 2z_I. \end{aligned} \tag{56}$$

The quadratic equation can then be solved for $\delta(|E|^2)$:

$$\delta_\pm = -\frac{c_1}{2} \pm \sqrt{\frac{c_1^2}{4} - c_2}. \tag{57}$$

Hence, there are two connected branches of the nullcline. Furthermore, for $\delta_{\pm}(|E|^2)$ to be real, the discriminant must be non-negative:

$$\frac{c_1(|E|^2)^2}{4} - c_2(|E|^2) \geq 0. \tag{58}$$

This condition imposes an upper bound on $|E|^2$, denoted by $|E|^2_{\max}$, beyond which no real solution for δ^* exists.

We then define the critical manifold $\mathcal{S}$ as the set of all points (E, δ) satisfying the nullcline equations:

$$\mathcal{S} = \left\{ (E^*(|E|^2), \delta^*(|E|^2)) \;\middle|\; 0 < |E|^2 \leq |E|^2_{\max} \right\}. \tag{59}$$

Here, $|E|^2$ acts as a continuous parameter parametrizing the manifold and forming a one-dimensional curve in (E, δ)-space, with two connected branches corresponding to δ_+ and δ_-.

Now, linearizing f along the slow manifold gives

$$\dot{\delta E} = \frac{\partial f(E, \delta)}{\partial E}\bigg|_{E^*, \delta^*} \delta E + \mathcal{O}((\delta E)^2), \tag{60}$$

where the Jacobian is identical to Equation 46 excluding the last row and column. The analysis of the linearized system shows that the slow manifold is locally stable along one upper and one lower branch, while the connecting branch is unstable and repelling (cf. Figure 6). The transition points from stable to unstable and vice versa are called fold points, where normal hyperbolicity breaks down [14].

Since the system dynamics exclude the ODE for δ, the critical manifold $\mathcal{S}$ cannot be modified by changing the parameters μ_α and δ_0. Choosing either δ_0 or μ_α as a bifurcation parameter only changes the δ-nullcline and thus controls the position of the fixed point, also called the Continuous Wave (CW) solution.

Another possible choice of control parameter is the injection Y_0, which, according to Equation 53 and Equation 57, scales $|E^*|^2$ and δ^* quadratically and thus rescales $\mathcal{S}$.

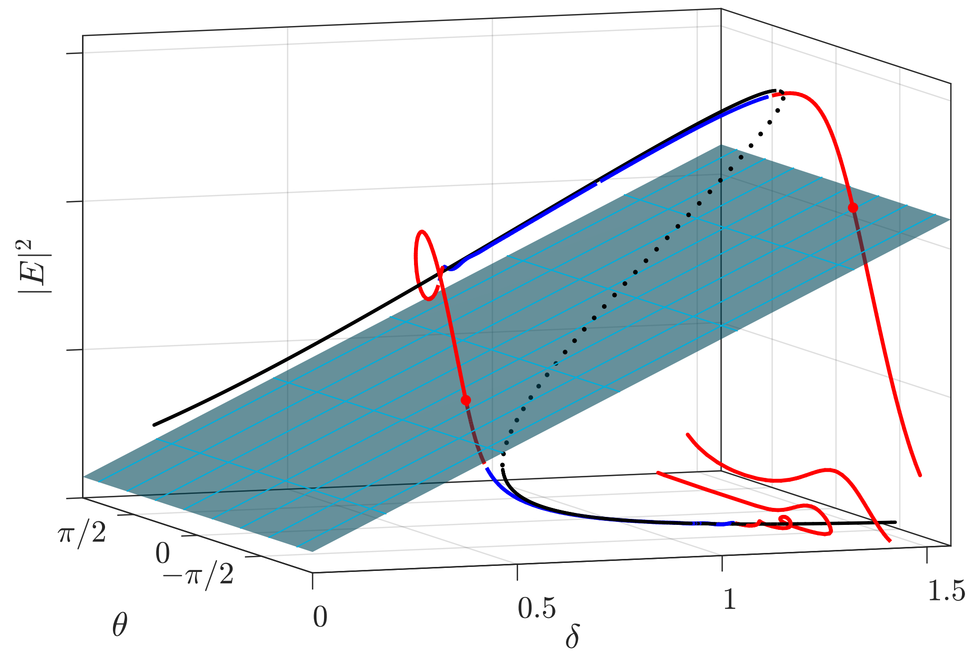

Figure 6: 3-dimensional phase space $(\theta, \delta, |E|^2)$ with trajectory for the relaxation oscillation regime. The fast free parts of the orbit are colored red while the slow parts enslaved to the nullcline are blue. The unstable parts of the black E-nullcline are dotted while the stable parts are solid lines. The phase invariant δ-nullcline is a plane in 3 dimensions.

For the chosen parameter set, the system has only one fixed point, since only the parameter μ_α is varied. It represents the slope of the δ-nullcline. This fixed point on the Continuous Wave branch is stable only if the δ-nullcline intersects a stable part of the critical manifold. Otherwise, it is unstable.
Since in this thesis only solutions with $\delta_0 < 0$ are considered, there is only one fixed point. For positive δ_0, up to three fixed points can appear.
The transition between the stable CW fixed point and the sudden onset of large-amplitude periodic relaxation oscillations is referred to as a canard explosion. In this case, the two Canard explosion candidates correspond to the transitions of the CW branch from a stable to an unstable regime at the two fold points of the critical manifold.
In particular, the stable parts of the slow manifold possess pairs of complex conjugate eigenvalues, which explain the tail oscillations in the excitable state and the relaxation oscillations seen in Figure 6. These phase rotations are most likely a result of the Kerr effect introduced by the term $i(|E(t)|^2 - \delta(t))E(t)$.
For the numerical simulations, the parameters that remain fixed throughout the thesis are chosen as follows:

- $\delta_0 = -0.1070$,
- $h = 2$,

- $\eta = 0.7$,
- $\varphi = 0$,
- $Y_0 = 0.25$,
- $s = 0$.

For the non-delayed case, the thermal time scale γ is set to 0.01, ensuring scale separation. The thermal coefficient μ_α is the only bifurcation parameter varied in this thesis.

8.1 Periodic solutions

As discussed in the previous part, relaxation oscillations exist as a fundamental periodic solution of the system if the δ-nullcline intersects the unstable part of $\mathcal{S}$. By varying the slope via the parameter μ_α, one observes that the period is monotonically increasing for larger μ_α.

Also, between c) and d) in Figure 7, not only does the periodic orbit shrink, but its amplitude also decreases, so that the solution is no longer a relaxation oscillation but a sinusoidal solution around the CW fixed point.

As is discussed later, this corresponds to a solution born out of a supercritical Hopf bifurcation of the CW fixed point, which clearly corresponds to the Canard phenomenon.

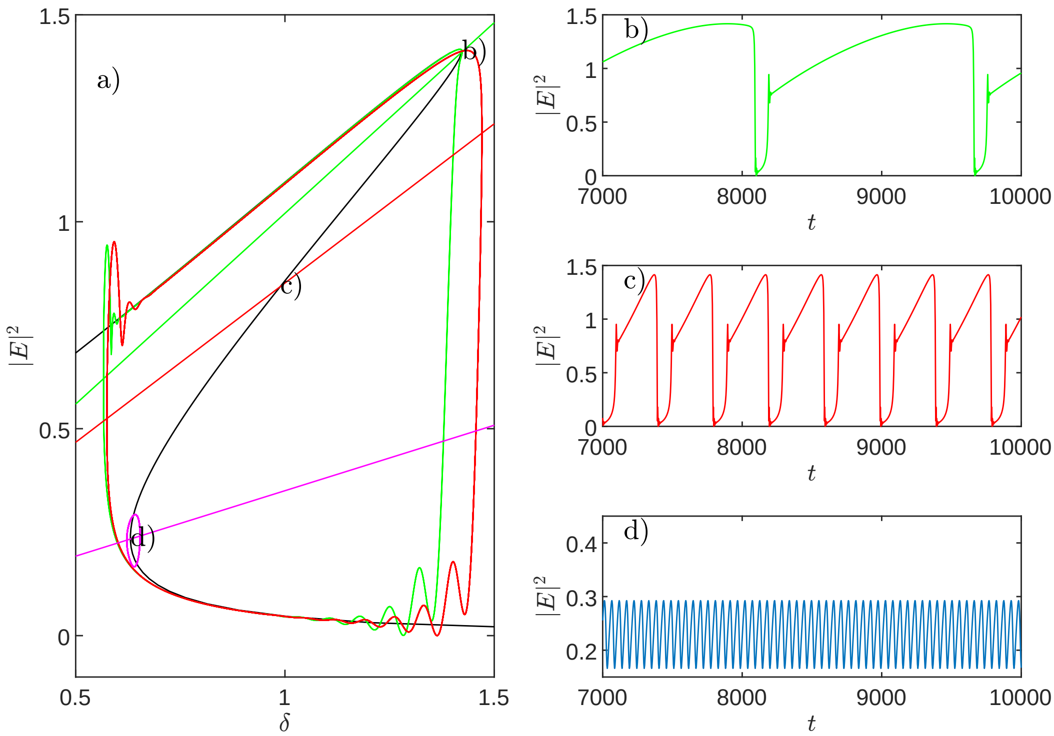

Figure 7: a) Phase space $(\delta, |E|^2)$ with critical manifold and the δ-nullcline for varied μ_α. b) Relaxation oscillations with large period for $\mu_\alpha = -3.1613$, c) relaxation oscillations with a shorter period for $\mu_\alpha = -1.2995$, and d) small-amplitude short-periodic solutions after the Hopf bifurcation for $\mu_\alpha = -1.0850$.

8.2 Excitability

In this section, we investigate noise-induced periodic solutions near the onset of instability. Therefore, we introduce white Gaussian noise with standard deviation σ to the E-field, which can push the orbit beyond the fold point such that the orbit completes one relaxation cycle. According to Pikovsky and Kurths [7], there exists an optimal noise value for so-called coherence resonance, which minimizes the normalized fluctuations $R(\sigma)$ of the interspike interval (ISI) Δt between excitations. These fluctuations are defined as

$$R(\sigma) = \frac{\sqrt{\mathrm{Var}(\Delta t(\sigma))}}{\langle \Delta t(\sigma) \rangle}. \tag{61}$$

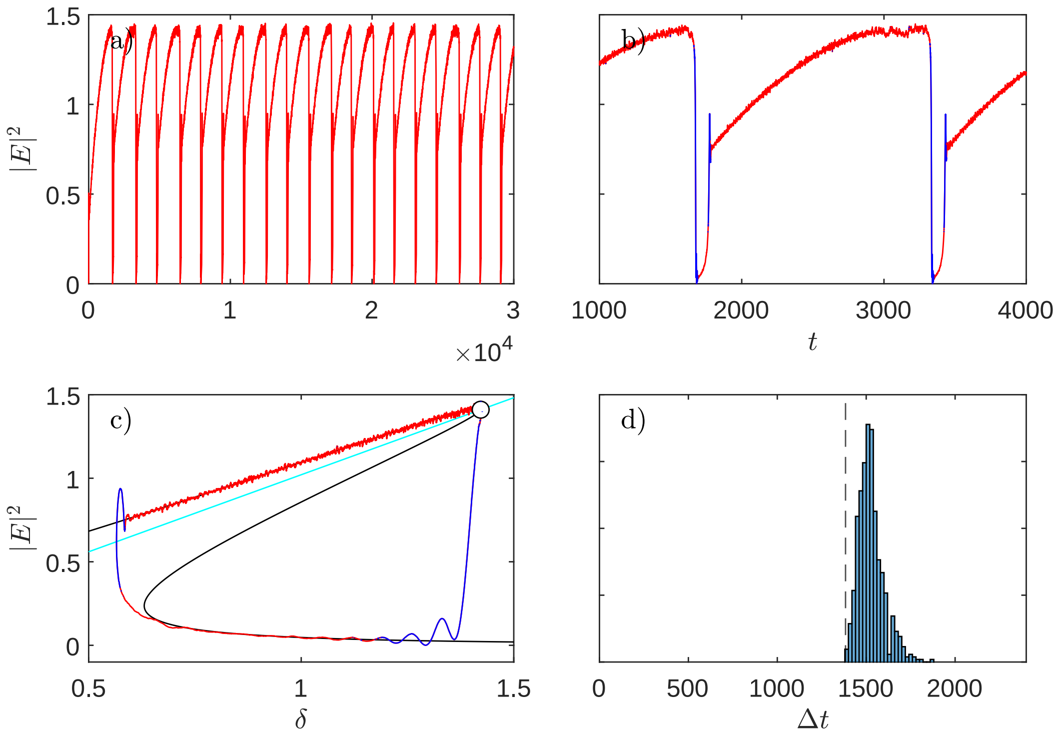

Figure 8: Subthreshold dark excitability at $\mu_\alpha = -1.0843$ for noise amplitude $\sigma = 0.003$. a) Time trace of many pulses. b) Single pulse. c) Phase space diagram with one closed pulse orbit. The white dot indicates the CW solution before the onset of instability. d) Histogram distribution of interpulse intervals (ISI) Δt.

In Figure 8, direct numerical simulations reveal behavior for small noise values before the onset of the relaxation regime at the stable CW fixed point (cf. Figure 8c). In Figure 8a, a time trace of the E-field intensity shows excitations caused by noise, while Figure 8b shows a single pulse, illustrating the enslaved dynamics and the fast free dynamics after overcoming the potential barrier. Figure 8d shows the distribution of the interpulse intervals Δt, which is Poisson-like and has a minimal value which is near the period of the stable relaxation oscillation immediately after the instability of the Continuous Wave (CW) solution but.

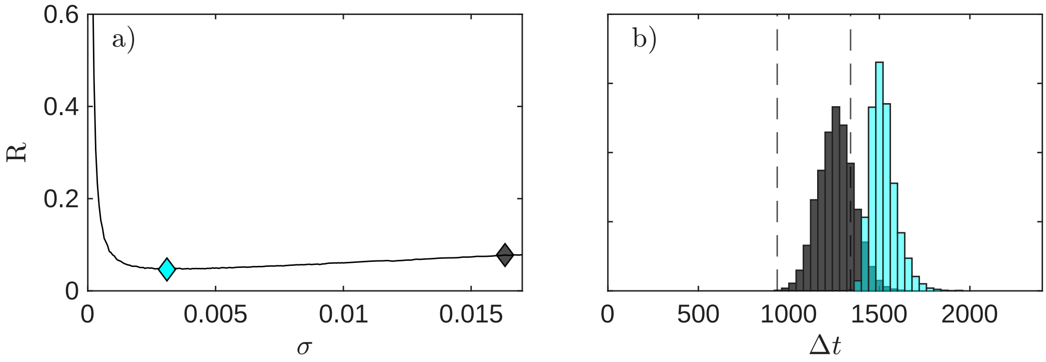

Figure 9: a) Normalized variance R vs. the noise amplitude. The diamonds correspond to the histograms shown in b) for the optimal $\sigma = 0.003$ and a suboptimal $\sigma = 0.0163$. b) Histograms of inter-pulse intervals for the optimal and suboptimal noise values.

In Figure 9a, the relative fluctuations as a function of the noise amplitude show a minimum value or rather, an interval of minimum values where R is minimized. In Figure 9b, the two distributions for the optimal noise value around $\sigma = 0.003$ and a suboptimal value highlight large differences in the sharpness and mean value of the pulse duration Δt. In this case, the coherence is rather low since the minimum is shallow. It is important to note that it is not the mean ISI that is minimized, but only the fluctuations. Thus, only the regularity of the pulses reaches its maximum at $\sigma = 0.003$. For higher noise values immediate reexcitation is possible but is not regular enough to minimize R.
The second point for excitability to occur is right before the Canard explosion, immediately after the first Hopf bifurcation of the CW branch. As depicted in Figure 7d, after the Hopf bifurcation, stable small-amplitude limit cycles appear. Approaching the Canard explosion in $(\mu_\alpha, \langle |E|^2 \rangle)$, these periodic solutions undergo several fold and period-doubling bifurcations (cf. Figure 10a and b). An example of such a period-doubling case for a $T_1 = 78.717$ periodic solution is displayed in Figure 10 c), where this solution becomes unstable and a $2T_1$ periodic solution is born on top of the original cycle, after a Floquet multiplier crosses the unit circle in the complex plane at -1.

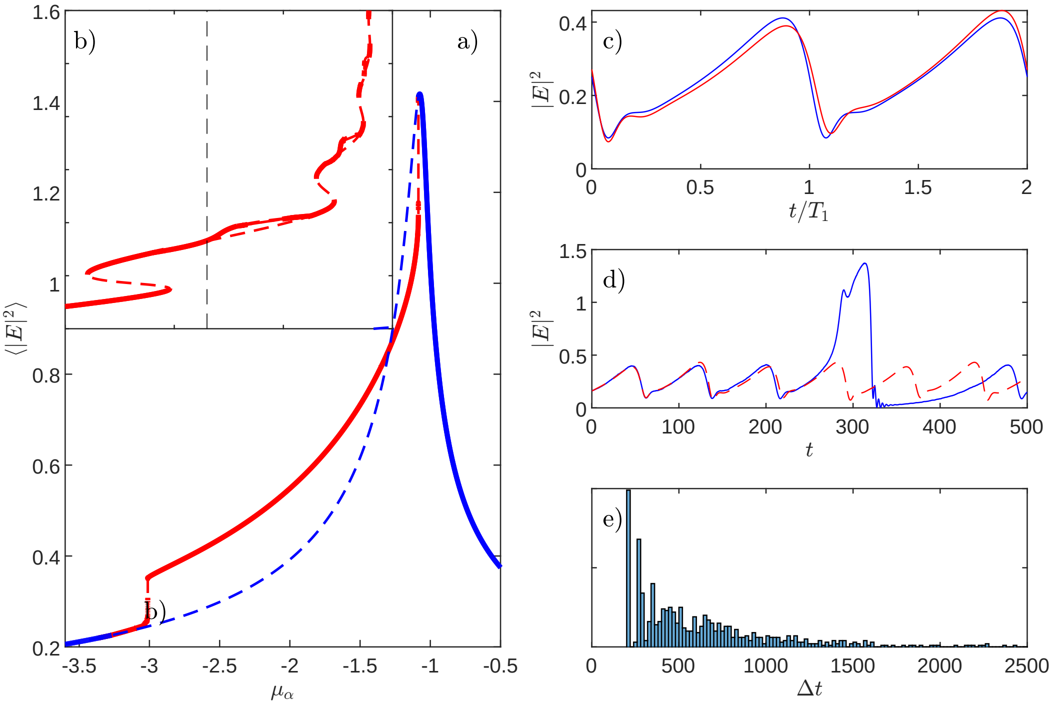

Figure 10: a) Bifurcation diagram with the blue CW branch and the orange periodic branch. The unstable parts are denoted with dashed lines. b) Onset of the Canard with multiple fold and period-doubling bifurcations. c) Unstable period $T_1 = 78.7173$ solution (blue) and stable period $2T_1$ solution at $\mu_\alpha = -3.0270$. d) Bright excitability on top of the period $2T_1$ solution for noise amplitude $\sigma = 0.001$, with the corresponding distribution of inter-pulse intervals Δt shown in e).

Since the Hopf bifurcation occurs sufficiently far from the Canard explosion, an unreasonably large amount of noise is needed to induce thermo-optical pulses (TOP) from the stable CW fixed point. Thus, the system can be excited more efficiently from the small-amplitude periodic attractor at the onset of the Canard branch. In Figure 10 d), we observe a TOP excitation that originates from the $2T_1$ stable periodic orbit under small noise.

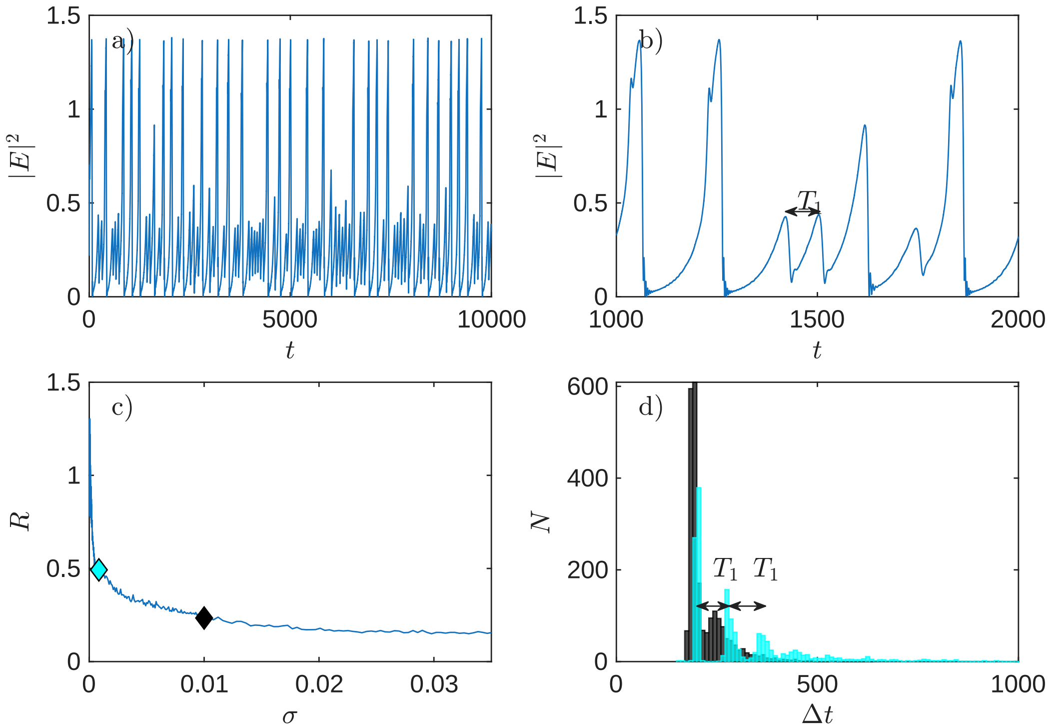

Figure 11: a) Time trace of TOPs for $\sigma = 0.001$ and a zoomed-in version in b). c) Normalized variance of the ISI as a function of σ. Diamonds indicate the noise values corresponding to the histogram in d) for $\mu_\alpha = -3.015$.

In the case of TOP excitations, no coherence resonance is observed, as the function $R(\sigma)$ decreases monotonically and therefore does not exhibit a local minimum (cf. Figure 11). In contrast to the dark excitations, the pulse amplitudes display a broader distribution, which exhibits less variation and becomes more pronounced with increasing noise intensity with a clear cutoff at the intrinsic excursion time of the pulse.

For small noise amplitudes, the noise-induced pulses are separated by interpulse intervals of $n{\cdot}T_1$, since excitability (cf. Figure 10 b)) only allows pulses to be initiated at the maxima of $|E|^2(t)$ along the underlying periodic attractor. This effectively generates mixed-mode oscillations (MMO), which cannot be found in the system without noise. For a different parameter set actual MMOs have been observed [4]. Consequently, pulse generation is phase-locked to the oscillatory background dynamics.

8.3 Subthreshold chaos

As discussed previously, the section in parameter space between the Hopf bifurcation and the Canard explosion exhibits rich behavior, including folds and period-doubling bifurcations. Interestingly, the Canard explosion does not follow directly after the Hopf bifurcation of the CW branch, in contrast to the other Hopf bifurcation. Especially in the vicinity of the Canard explosion, successive period-doubling bifurcations unfold into a cascade that ultimately results in chaotic dynamics (cf. Figure 12). This behavior has already been studied for a modified van der Pol–FitzHugh–Nagumo model [18].

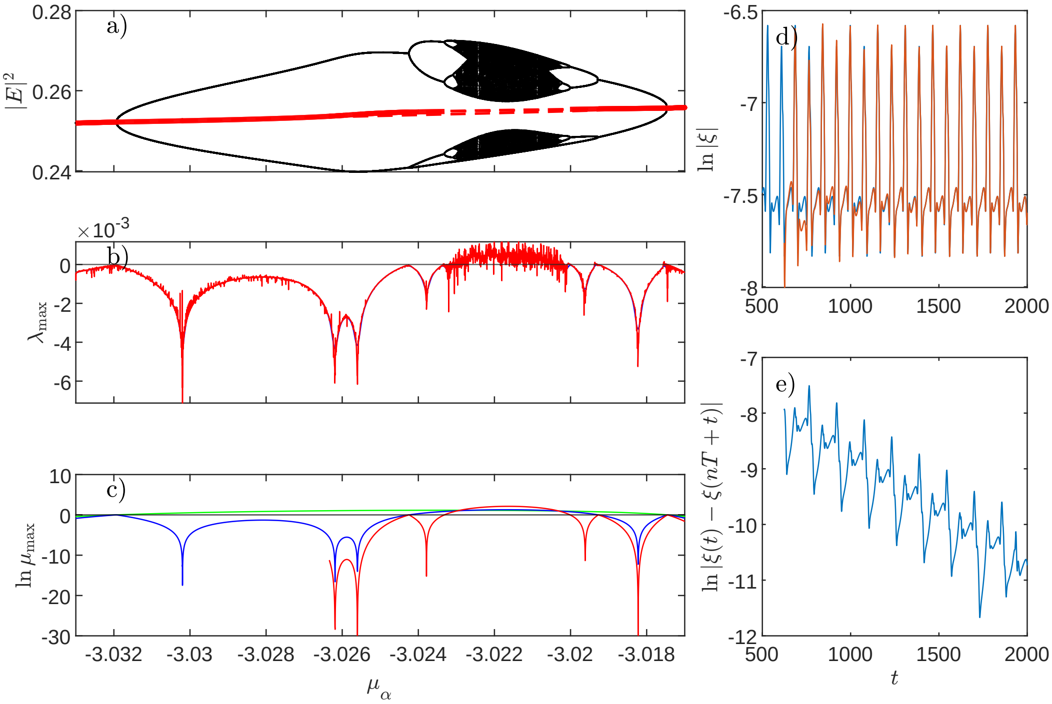

Figure 12: a) Orange branches are the branches of the period-1, period-2, and period-4 solutions. The Feigenbaum diagram is obtained by direct numerics. b) Directly computed Lyapunov exponent $\lambda_{\max}$ compared to the maximum Floquet multiplier $\ln \mu_{\max}$, d) ln of the perturbation and the shifted perturbation by $5T$ at $\mu_\alpha = -3.0285$, e) ln of the difference between the shifted and non-shifted perturbation.

To characterize this chaos, the maximum Lyapunov exponent $\lambda_{\max}$ can be used, which measures the time evolution of the difference $\xi = x_1 - x_2$ between two trajectories with slightly different initial conditions $\xi_0 = x_{1,0} - x_{2,0}$ in the vicinity of the attractor [10] as

$$|\xi| = |\xi_0| \exp\{\lambda_{\max} t\}. \tag{62}$$

where $\lambda_{\max}$ is defined as

$$\lambda = \lim_{t\to\infty} \lim_{|\xi_0|\to 0} \frac{1}{t} \ln \frac{|\xi(t)|}{|\xi_0|}. \tag{63}$$

For non-chaotic invariant sets, the difference between two initially closely separated trajectories usually decreases, resulting in a negative Lyapunov exponent. For chaotic attractors, the distance between orbits actually increases [10].
In order to compute the Lyapunov exponent, Equation 63 is numerically impractical, as trajectories follow Equation 62 only in the range of the attractor. After a finite time, this behavior can no longer be described accurately by this equation. Therefore, the exponent is obtained numerically by subtracting two solutions with slightly different initial conditions ξ_0 and computing the slope of $\ln \xi$ to estimate the Lyapunov exponent.
However, this is extremely difficult because numerically the initial conditions may not be settled on the attractor. Consequently, one can shift the difference by the period T of the solution n times, as depicted in Figure 12 d). Then, taking the difference and computing the average slope yields a quantity proportional to $\lambda_{\max}$. To show this, we observe that

$$\xi(t) - \xi(t - nT) = \exp\{\lambda t\} \left(1 - \exp\{(-\lambda nT)\}\right) \xi_0 \tag{64}$$

holds, where $\lambda \in \mathbb{C}^{3\times 3}$ in this representation. For large times, the largest eigenvalue $|\lambda|$ dominates and determines the behavior of the perturbation. We distinguish two cases regarding the sign of $\lambda_{\max}$:
Case I: ($\lambda_{\max} > 0$) For large enough n, $\exp\{(-\lambda_{\max} nT)\} \ll 1$, and the expression in Equation 64 reduces to $\xi_0 \exp\{\lambda t\}$, of which the norm can be taken. Hence, the final formula for the Lyapunov exponent is

$$\lambda_{\max} = \left\langle \frac{d}{dt} \ln \frac{|\xi(t) - \xi(t - nT)|}{|\xi_0|} \right\rangle = \left\langle \frac{d}{dt} \ln |\xi(t) - \xi(t - nT)| \right\rangle. \tag{65}$$

Case II: ($\lambda_{\max} < 0$) For large enough n, $1 \ll \exp\{(-\lambda_{\max} nT)\}$, and the expression in Equation 64 becomes $-\xi_0 \exp\{\lambda_{\max}(t - nT)\}$. Taking the absolute value, dividing by $|\xi_0|$, and performing the derivative of the ln again leads to Equation 65.
One must explicitly calculate the average since $\ln |\xi(t) - \xi(t - nT)|$ periodically fluctuates around the ideal linear function. This formula is also helpful for analyzing chaotic solutions. In this case, it is inaccurate to refer to T as the period. Rather, T should be interpreted as the time difference between maxima or minima of $x(t)$, provided one averages over enough intervals that do not deviate too much.
As seen in the derivation, Floquet theory is closely related to the concept of Lyapunov exponents, since Floquet multipliers also measure perturbations of periodic orbits and are thus related to Lyapunov exponents via $\mu = \exp\{\lambda\}$. As seen in Figure 12b,c , the ln of the maximal Floquet multipliers behaves similarly to the numerically computed maximal Lyapunov exponents.

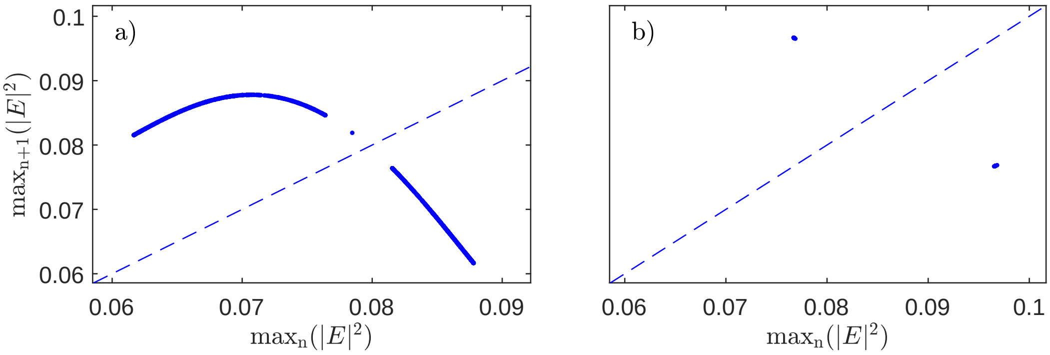

Figure 13: Map that relates the maximum amplitude $\max_{n+1}(|E|^2)$ to the previous maximum amplitude $\max_n(|E|^2)$ for a) a solution inside the chaotic attractor with $\mu_\alpha = -3.022$, and b) a solution with two periods $\mu_\alpha = -3.028$. The dashed line denotes the identity map, where maxima for a solution of one period would lie.

Another characteristic property of chaos is that the map between maxima $\max_n(|E|^2)$ and $\max_{n+1}(|E|^2)$ behaves like a continuous function (cf. Figure 13a), rather than discrete points in $(\max_n(|E|^2), \max_{n+1}(|E|^2))$, in contrast to periodic solutions or fixed points (cf. Figure 13b).

9 Impact of time-delayed feed

For the case where the distance of the feedback mirror at the end of the large cavity to the second Bragg mirror is much larger than the length of the microcavity, the round trip in the external cavity cannot be ignored. Therefore, the system is described by the full thermal KGTI system with delay τ, as described by Equation 25. Consequently, the system exhibits new dynamical behaviors arising from the interplay between the slow thermal time scale γ and the external-cavity delay τ. In the following numerical simulations, the delay τ is set to 100.

9.1 τ-periodic solutions

We now investigate τ-periodic solutions induced by delayed feedback in the slow-fast system defined by Equation 25. These solutions extend the relaxation oscillations found in the non-delayed system and reveal global dynamical features beyond the local slow manifold and the small periodic/chaotic attractor.

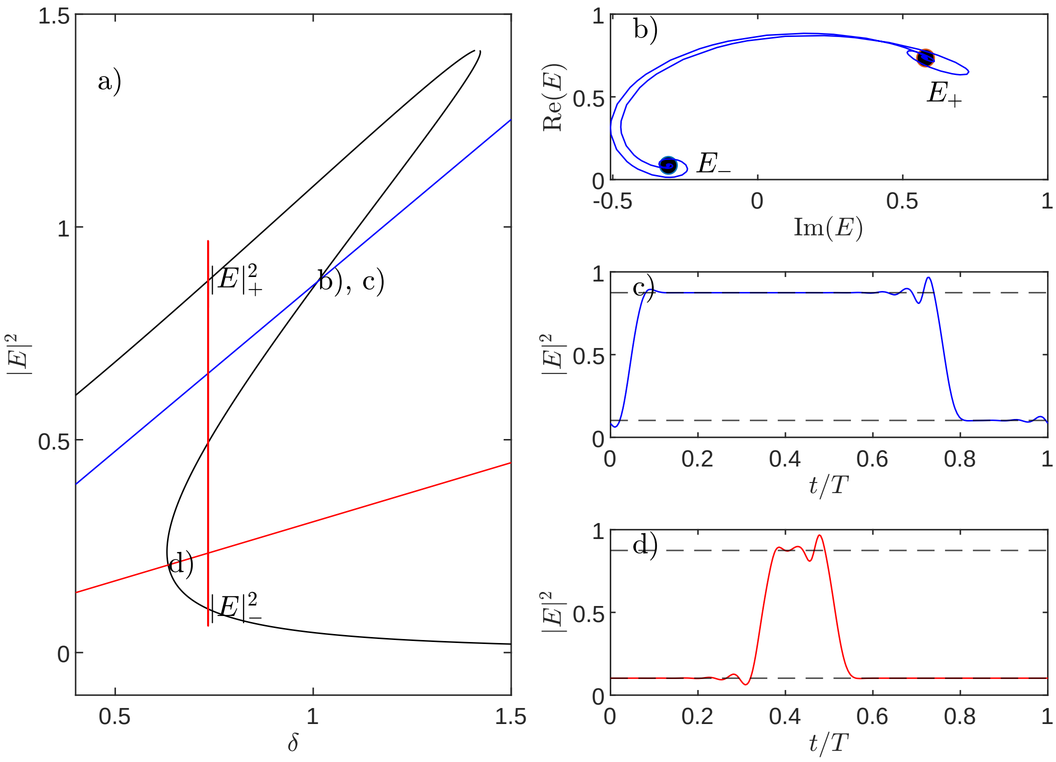

Figure 14: a) Phase space with critical manifold, showing lower and upper parts $|E|^2_-$ and $|E|^2_+$, and δ nullcline for different stable $T \approx \tau$-periodic solutions with $\gamma = 10^{-4}$. Stability of the periodic solutions is determined via numerical path continuation. b) Reduced phase space at $\delta = \langle \delta \rangle$. c) Solution for $\mu_\alpha = -3.502$. d) Solution for $\mu_\alpha = -1.283$. The dashed lines denote the position of $|E|_+$ and $|E|_-$.

For $\gamma \ll 1$ and in the regime $\frac{1}{\gamma} \ll \tau$, the slow variable δ evolves on a timescale much longer than the delay. This allows us to treat δ as quasi-stationary during the fast dynamics of E. Using a procedure analogous to the non-delayed case, one recovers the relaxation oscillations for small perturbations in E, with identical local slow manifold stability. Notably, even large perturbations do not qualitatively change these solutions.

The introduction of delayed feedback terms $E(t-\tau)$ and $Y(t-\tau)$, chosen sufficiently large in the initial condition, generates strong delayed interactions. This produces oscillations with period $\tau+\delta t$. Remarkably, these τ-periodic solutions persist beyond the first Hopf bifurcation and the subsequent Canard explosion. In particular, they correspond to cycles connecting the stable branches of the critical manifold, which can be seen in Figure 14.

With the approximation $E(t-\tau) \approx E(t)$, the delay differential equations can then be reduced to the form:

$$\begin{aligned} \dot{E} &= f(E,\delta) = \Big[h\frac{\eta}{1+\eta} - 1 + i\left(|E|^2 - \delta\right)\Big]E + h\frac{\sqrt{1-\eta^2}}{1+\eta}Y_0, \\ \dot{\delta} &= \gamma g(E,\delta) = \gamma(\delta_0 - \delta_c - \mu_\alpha |E|^2). \end{aligned} \tag{66}$$

The reduced system can again be approximated by the critical manifold defined by $f(E,\delta) = 0$ from the non-delayed case. It is then observed that the τ-periodic solutions revolve around the two stable branches of the critical manifold, where a balance condition for the critical $\delta_c = \langle\delta\rangle = \delta_0 - \mu_\alpha\langle|E|^2\rangle$ can be obtained. Therefore, considering the fast jump between the two stable branches, the approximate equations for the displacement $\Delta\delta$ during the jump and the displacement in the E direction are:

$$\Delta\delta = \int_{t_-}^{t_+} g(E,\delta)\,dt, \qquad dE = f(E,\delta)\,dt \tag{67}$$

In the E direction, the jump is almost instantaneous. Hence δ can be assumed to be stationary. Also, the displacement $\Delta\delta$ can then be assumed to be 0 in leading order. So, the balance condition can be expressed as the real part of the complex path integral connecting the branches E_+ and E_-:

$$\mathrm{Re}\int_{E_-(\delta_c)}^{E_+(\delta_c)} \frac{g(E,\delta_c)}{f(E,\delta_c)}\,dE = 0. \tag{68}$$

E_- and E_+ are also fixed points in the reduced system without delay, that can only be connected with present delay adding infinetly more dimensions, so that the τ delayed feedback term pushes the orbit beyond the separatrix (i.e., the unstable part of the critical manifold) and can form an actual finite-periodic solution. Additionally, the connecting orbit can, in first order, be approximated as a straight line. So the integral equation reads:

$$I(\delta_c) = \int_0^1 \Big(\mathrm{Re}\Big(\frac{g(E(s,\delta_c))}{f(E(s,\delta_c))}\Big)\,\mathrm{Re}(v) - \mathrm{Im}\Big(\frac{g(E(s,\delta_c))}{f(E(s,\delta_c))}\Big)\,\mathrm{Im}(v)\Big)\,ds = 0, \tag{69}$$

where the straight line is parametrized by s with

$$E(s) = E_- + v\,s, \qquad v = E_+ - E_-. \tag{70}$$

This approximation is only valid far enough away from the global bifurcation at the upper fold point. At the fold point (cf. Figure 15a), the orbit detaches from the lower part E_- and the path approximation that involves E_- as one endpoint does not hold anymore. Also, as seen in Figure 14b, $E(s)$ is actually a curved connection, which leads to further uncertainty regarding the approximate analytic solution. Unfortunately, imposing the constraint $I(\delta_c) = 0$ in path variational methods by Lagrange multipliers introduces an extra degree of freedom, making the problem not readily solvable using this method. Furthermore, since the branches E_- and E_+ are independent of μ_α, δ_c remains constant. Considering these limitations, the analytic approximate solution in Figure 15b is a good fit for the branch of these solutions.

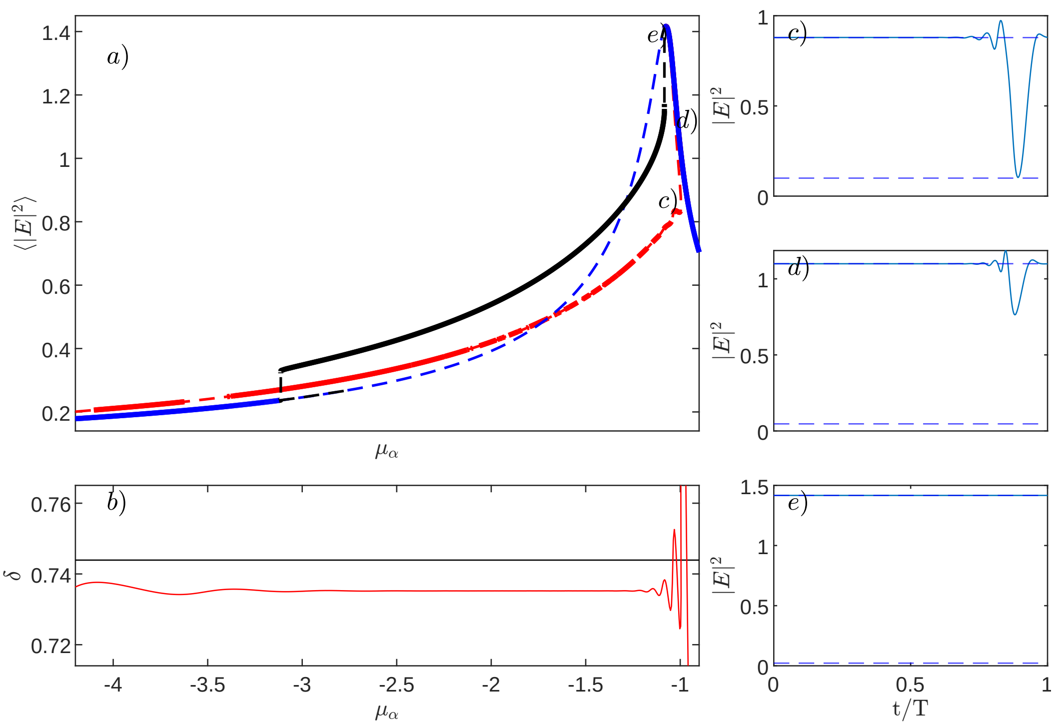

Figure 15: a) Bifurcation diagram of the thermal KGTI system with $\gamma = 10^{-5}$, Blue: CW Solution, Red: delay-induced switched state, Black: Relaxation Oscillations. b) Analytic solution for δ_c and actual solution. c), d), e) Different profiles of the switched state branch.

Moreover, the solutions have two conditions: they must stay most of the time in the slow dynamics at either E_- or E_+, and they must fulfill the time-average condition $\langle|E|^2\rangle = \frac{\delta_0 - \delta_c}{\mu_\alpha}$. As δ_c has been found to be mostly constant in μ_α, with increasing μ_α the norm also increases, therefore forcing the τ-periodic solution to be a temporally localized pulse for smaller μ_α and a dark temporally localized pulse for larger μ_α

(cf. Figure 14c, d).

These types of solutions in delayed slow-fast systems are also referred to as *delay-induced switched states* [19]. Moreover, these switched states are not always stable. As depicted in Figure 15a, the branch becomes irregularly unstable in supercritical torus bifurcations. At point c) in Figure 15, the orbit starts to detach after a fold bifurcation from the lower branch E_- and evolves into an unstable cycle also with period $\approx \tau$ (cf. Figure 15c) that only reconnects to E_+. Following the branch, the amplitudes become smaller. Eventually it merges into the CW branch at the supercritical Hopf bifurcation that also births the relaxation oscillations. Furthermore, an additional pair of complex conjugate eigenvalues of the CW have imaginary parts which indicate a period $\approx \tau$. Thus, the CW branch in the infinite-dimensional delayed system produces more than one cycle out of the Hopf bifurcation of the CW, albeit in different parameter direction. In conclusion, the Hopf bifurcation is observed to be supercritical for the relaxation oscillations but subcritical for the switched state.

As discussed previously, the large relaxation oscillations are also preserved in the limit, as the delay time is much smaller than the time the orbit spends on the slow branches of the critical manifold. In the $\tau \ll 1$ limit, the small-amplitude periodic orbit emerging from the supercritical Hopf bifurcation undergoes a sequence of period-doubling bifurcations and folds before the onset of the canard explosion. When delay is introduced, this secondary bifurcation scenario disappears. This can be attributed to the stabilizing effect of delay on the Hopf limit cycle. In particular, the delay introduces memory effects that average growing perturbations over a finite time interval, thereby suppressing the flip instability responsible for period doubling. Later on, this effect is important when examining the excitability cases. Similarly to the non-delayed case, the large relaxation oscillations reconnect to the CW branch via a supercritical Hopf bifurcation.

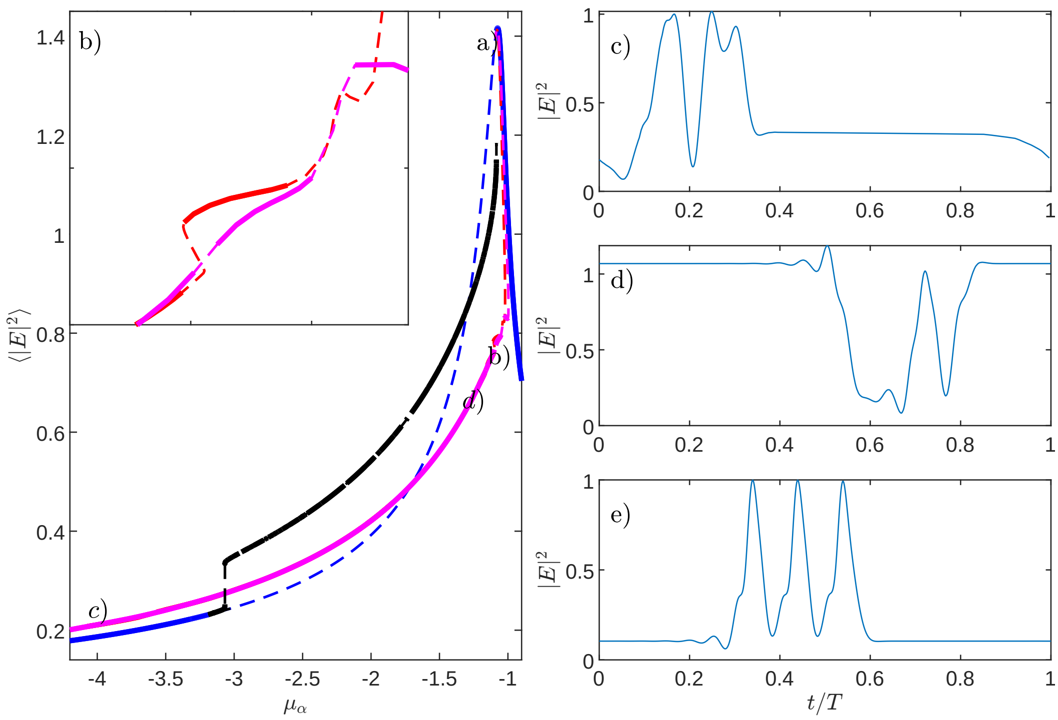

Figure 16: a) Bifurcation diagram of the thermal KGTI system with $\gamma = 10^{-4}$. Blue: CW Solution, Red: first delay-induced switched state, Magenta: second delay-induced switched state, Black: Relaxation Oscillations. c), d) Different profiles of the second switched state branch. e) Three-pulse switched state for $\gamma = 10^{-6}$ for $\mu_\alpha = -5$.

Reducing the thermal time scale γ to 10^{-4} preserves the structure of the bifurcation diagram, as can be seen in Figure 16. Here, a second delay-induced switched state can also be observed, which makes two roundtrips between E_- and E_+ but has the same period as the first switched state. This second switched state can also be observed for $\gamma = 10^{-5}$.

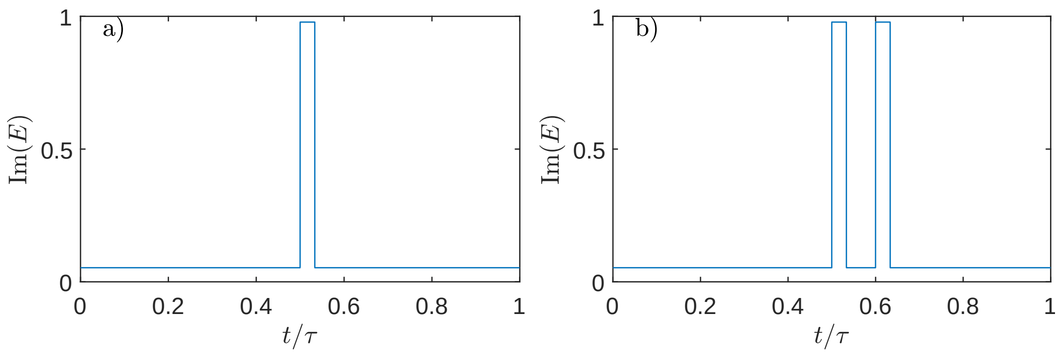

Figure 17: a) Initial condition for the first kind of delay-induced switched state. b) Initial condition for the second kind of delay-induced switched state for the imaginary part of E.

Numerically, the switched state solutions can be obtained by using the initial condition in Figure 17a, where on top of the E_- branch at δ_c, a short pulse with the height of E_+ at $\delta = \delta_c$ is added, ensuring the feedback necessary to initialize the switched state solution.

Remarkably, solutions with two peaks on top of the E_- branch also exist if one uses a similar initial condition with two short pulses separated by a time Δt_r. Δt_r must be chosen on the order of the interpulse duration between the two peaks (cf. Figure 17b).

Since both solutions must satisfy the same integral condition from Equation 69, they do not differ significantly from the Hopf bifurcation in the $(\mu_\alpha, \langle|E|^2\rangle)$ space of the bifurcation diagram, as $\langle|E|^2\rangle$ is only a function of δ_c, which is the same for both solutions.

Repeating the process for more than two peaks did not result in solutions with more peaks for $\gamma = 10^{-5}$. However, if γ is one order of magnitude smaller, three-peak solutions can be observed in Figure 16e.

This can be attributed to the speed at which the delay merges tails and the speed at which the pulses stabilize. It seems that the ability to merge distinct pulses is inversely related to the magnitude of the thermal time scale. This mechanism is further examined in subsubsection 9.2.1.

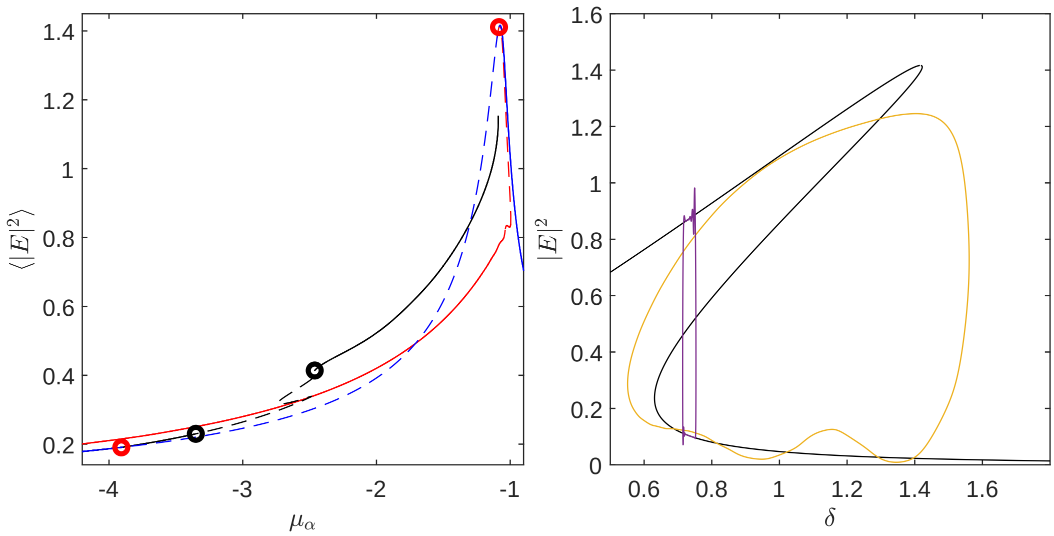

Figure 18: a) Bifurcation diagram of the thermal KGTI system with $\gamma = 10^{-3}$. Blue: CW Solution, Red: first delay-induced switched state, Black: Relaxation Oscillations. Red circles represent the Hopf bifurcations, and black circles represent Torus bifurcations. b) Phase space with critical manifold, switched state solution (black), and relaxation oscillation.

For $\gamma = 10^{-3}$, the time-scale separation breaks down, and the Canard explosion following the first Hopf bifurcation is no longer observed. Instead, the small-amplitude oscillations emerging from the first Hopf bifurcation evolve smoothly into the large-amplitude excursions that persist up to the second Hopf bifurcation point. At the second point, however, the Canard scenario still exists, probably due to the large distance between the arms of the critical manifold $\mathcal{S}$.

During this transition, the periodic solutions undergo a torus bifurcation, as multiple pairs of complex-conjugate Floquet multipliers cross the unit circle in the complex plane.

Moreover, the switched-state solutions exhibit significant variation in the δ-direction. Nevertheless, they continue to satisfy the underlying stabilization mechanism and bifurcate in the same way as for smaller γ.

9.2 Excitability for the DDE

In this section, we focus on the excitable states and solutions that can be obtained in a similar manner to section 2. With the delay now present, interactions between the delay-induced switched states and the relaxation oscillations are possible, leading to different kinds of noise-induced pulses, that are also referred to as *breathers* [20] and have been experimentally observed in other optical systems.

9.2.1 Bright excitability

For bright excitability to occur, a Canard bifurcation must exist at the lower Hopf bifurcation point. Therefore, the case $\tau \ll \gamma^{-1}$ guarantees a bright excitable regime. For $\gamma = 10^{-5} = 10^{-3} \cdot \tau^{-1}$, these bright excitable states exist.
Due to the strong interaction caused by the delayed feedback, once the orbit is pushed above the threshold, the interaction leads to approximately τ-periodic switching between E_- and E_+ until the solution settles at either E_- or E_+. This results in two different excitable states with two different periods.

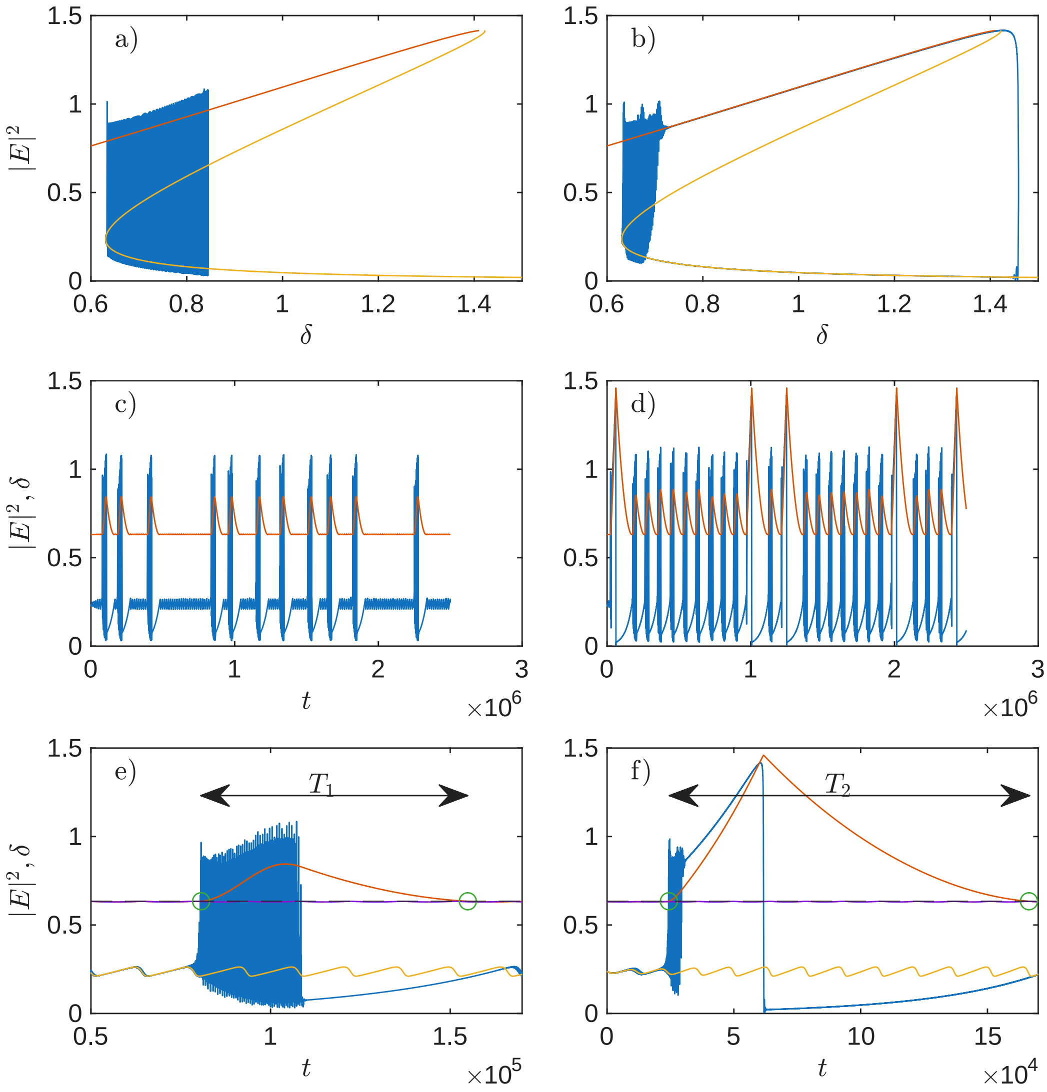

Figure 19: a), b) Phase space of the two different excitable solutions including the critical manifold. c), d) Time traces of $|E|^2$ and δ for $\sigma = 1.1525 \times 10^{-5}$ and $\sigma = 1.7914 \times 10^{-4}$. e), f) Single pulses for the respective noise values together with the small-scale Hopf solutions without noise ($|E|^2$: blue, δ: red).

As depicted in Figure 19, the T_2 solution corresponds to an actual relaxation oscillation that can also be observed in the case without delay. For the T_1 solution, the orbit settles at a point on E_- and does not reach the inflection point, thus not remaining as long in the slow δ dynamics.
Since there are at least two different kinds of pulses with two different periods, it is more appropriate not to consider the ISI but rather the actual pulse durations defined by passing a certain threshold.

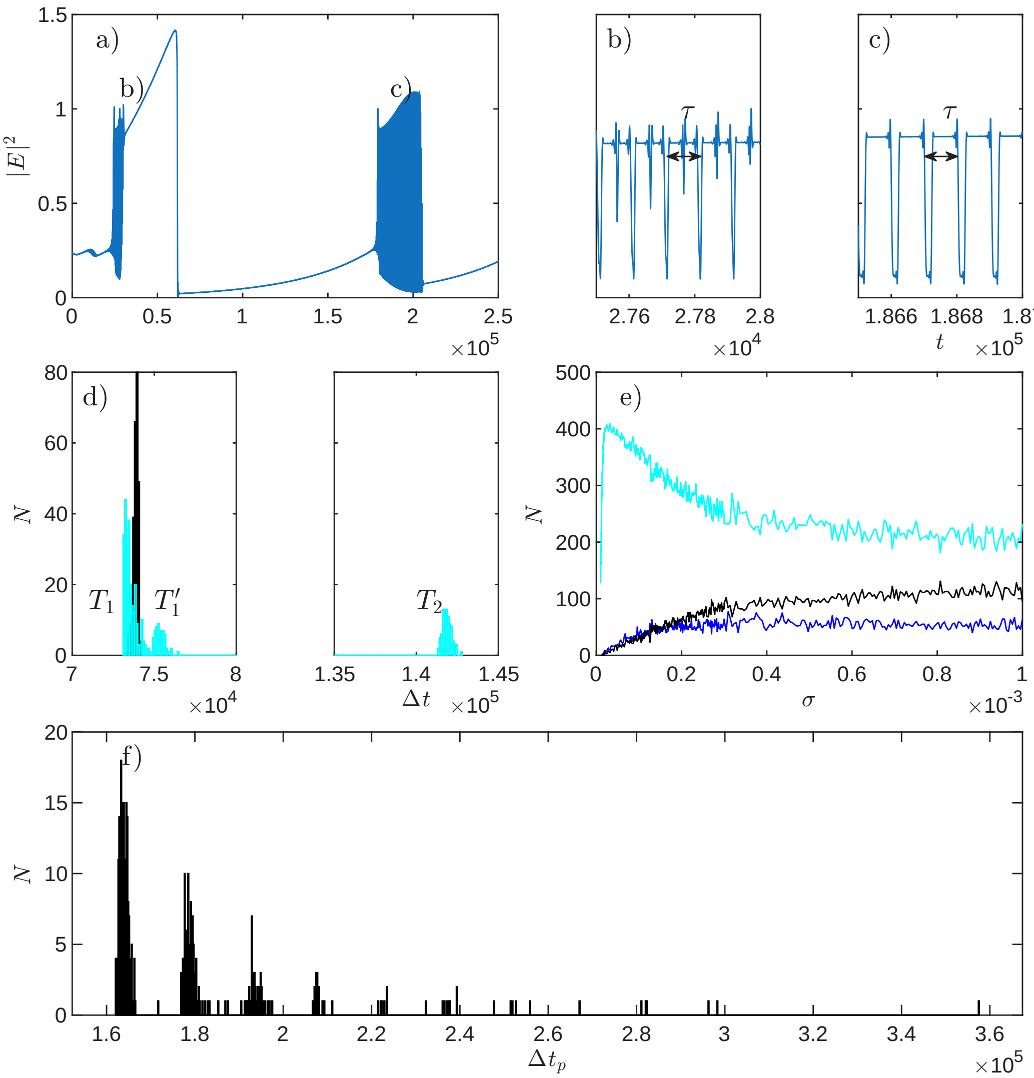

Figure 20: a) Time trace of the two kinds of bright excitable states. b) Dynamics of the two solutions during the interaction phase. c) Pulse durations for $\sigma = 1.2754 \times 10^{-5}$ (black) and $\sigma = 3 \times 10^{-4}$ (cyan). e) Number of pulse types as a function of the noise intensity (T_1: cyan, T_1': blue, T_2: black) for time $t = 4 \times 10^7$. f) Histogram of the distribution of inter-excitation times Δt_p for $\sigma = 1.2754 \times 10^{-5}$.

After performing numerical simulations for different noise values, a different type of excitable state with period T_1' can be distinguished, which closely resembles the T_1 solutions (cf. Figure 20).

Remarkably, the type of solution exhibited by the system depends on the noise strength σ. In Figure 20e, the pulse density for the different types is shown.

For very small noise, only a few pulses with period T_1 occur, reaching a maximum around $\sigma \approx 3 \times 10^{-5}$. For larger noise values, the T_1' and large T_2 solutions compete with the T_1 solution, such that at $\sigma \approx 4 \times 10^{-4}$ an equilibrium between the three kinds of solutions is observed. However, the small-amplitude T_1 and T_1' solutions dominate.

Similarly to the non-delayed case, the time between excursions Δt_p is phase-locked to the underlying periodic attractor, so that the inter-excitation time Δt_p is an integer multiple of the intrinsic period.
The offset in Figure 20f is due to the high threshold set to distinguish the pulses (cf. Figure 19e,f).

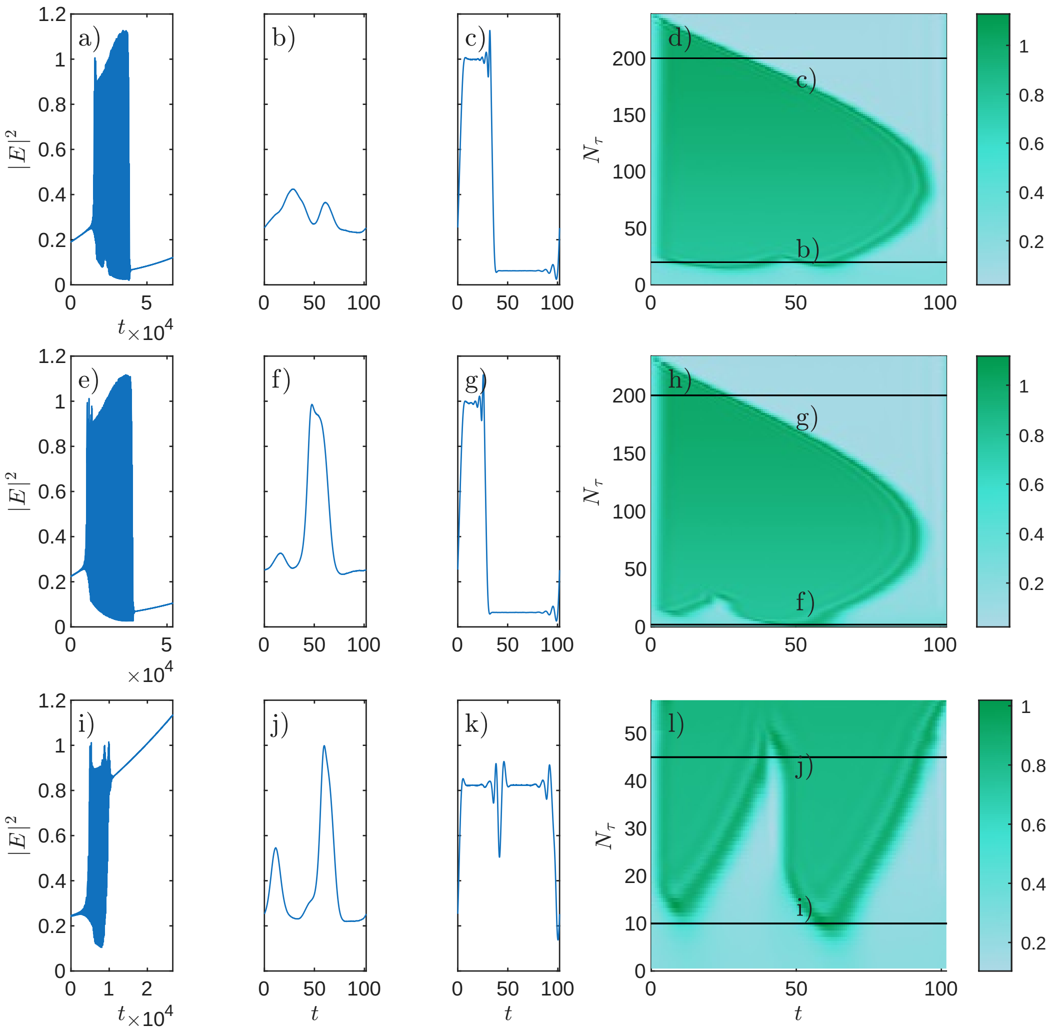

Figure 21: Interaction stages of the three kinds of bright excitable pulses. d), h), l) $|E|^2$ intensity during phases of length τ from the start to the end of the interaction stage. b), c), f), g), j), k) Different phase profiles corresponding to the interaction stages in a), e), i).

In Figure 21, the interaction can be divided into profiles of constant phase, i.e., where $E(t) \approx E(t-\tau)$. These profiles can be obtained by holding one front of the profile constant. This suppresses the slow drift speed, since the periods are $\gtrsim \tau$ and therefore not exactly uniform across all profiles.

All three types start with a phase that exhibits a two-pulse profile with large tail oscillations. These oscillations interact to form profiles resembling square waves with small tail oscillations.

Additionally, in all solutions there is a $\tau/2$ phase shift during the early interaction, such that the smaller pulse in the profile becomes the larger one.

This early interaction stage is shortest for T_1 and longest for T_2, since the pulses interact faster when they are closer together and less sharp.

For the T_2 solutions, the two pulses are at the maximal distance of $\tau/2$ and initially

smear out as if they were two independent pulses, merging only at a relatively late stage. This is also true for the T_1' solution. However, the second pulse is less sharp and therefore merges earlier.
As a result, the left and right tails of the resulting square pulse cannot interact strongly enough, leading to the same decay toward E_- as in the T_1 case.
Thus, two pulses within one τ-phase interact via their tails, smear out, and eventually merge. If the distance to the merged tail of the next τ-phase is sufficiently small, they can join and settle into the enslaved E_+ dynamics. If, however, this distance is too large, the merged pulse eventually shrinks and becomes bound to the enslaved E_- dynamics.

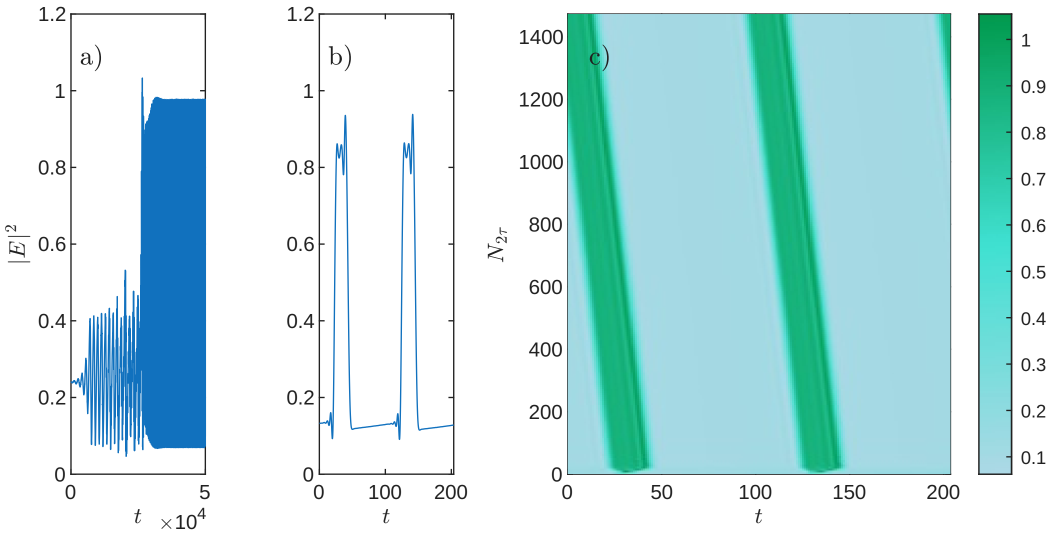

Figure 22: Interaction stage at the periodic attractor for $\gamma = 0.0001$: a) Time trace. b) Profile of a double phase. c) $|E|^2$ intensity during phases of length $\approx 2\tau$ from the start to the end of the interaction stage.

However, excitability is no longer observed for $\gamma = 10^{-4}$ and smaller values. In this regime, the Hopf bifurcation is followed by a canard bifurcation, in marked contrast to the case $\gamma = 10^{-3}$, where the Canard scenario disappears entirely for the lower fixed point originating from the CW branch.

Moreover, the delay-induced switched state exhibits a significantly larger basin of attraction. Small stochastic pulses coalesce more rapidly, while weaker modes are suppressed more efficiently. Consequently, for comparable noise intensities, substantially longer times are required to generate large-amplitude spikes on top of the underlying periodic solution.

As illustrated in Figure 22c, the relatively fast δ-dynamics inhibits long-range interactions between two large pulses separated by τ. As a result, the system converges toward the delay-induced switched state solution.

9.2.2 Dark excitability

Dark excitability refers to excitable states that result from perturbations of the upper fold point. In contrast to the lower fold point, all bifurcation diagrams retain the Canard scenario at the upper fold point for $\gamma = 10^{-5}, 10^{-4}$, and 10^{-3}, thus allowing noise-induced excitability to occur.

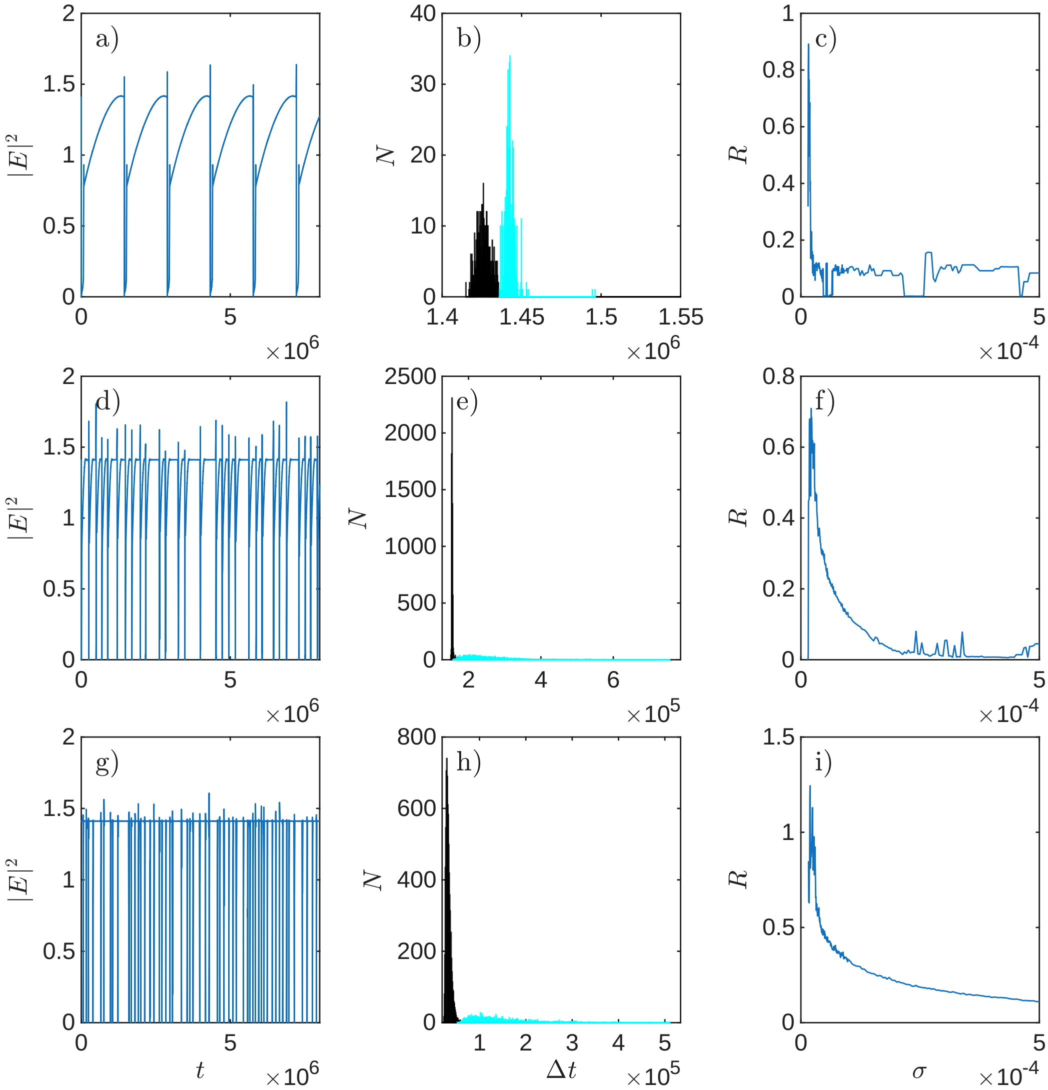

Figure 23: Noise-induced dark excitability at the CW fixed point for $\mu = -1.0837$ for $\gamma = 10^{-5}, 10^{-4}$, and 10^{-3}. a), d), g) Time traces of a series of pulses corresponding to the respective γ values with $\sigma = 5 \cdot 10^{-5}$. b), e), h) Histogram of the ISI for $\sigma = 2.9798 \cdot 10^{-4}$ (black) and $\sigma = 5 \cdot 10^{-5}$ (cyan). c), f), i) Relative fluctuations R as a function of the noise amplitude σ.

Dark excitability is observed for all investigated time scales. The pulse duration scales inversely with the thermal parameter γ, as expected, since the pulses correspond to relaxation oscillations. The relative fluctuations of the ISI also decrease with increasing noise strength σ. Since the noise fluctuates on the time scale of the

E field, for smaller thermal time scales the duration during which effective perturbations of the fixed point occur relative to the excursion time of a pulse is reduced. Consequently, for smaller γ, the decrease of $R(\sigma)$ is more pronounced. This effect can be observed in the pulse distribution for $\sigma = 5 \cdot 10^{-5}$ in Figure 23.
For $\gamma = 10^{-4}$, coherence resonance can be observed, as $R(\sigma)$ exhibits a small local minimum around $\sigma = 4 \cdot 10^{-4}$. This is consistent with the excitability pattern observed in the non-delayed case.
Similarly to the bright excitable pulses, an interaction stage also exists for dark pulses, during which the time-delayed feedback again leads to switching between E_- and E_+ with a period of approximately τ.

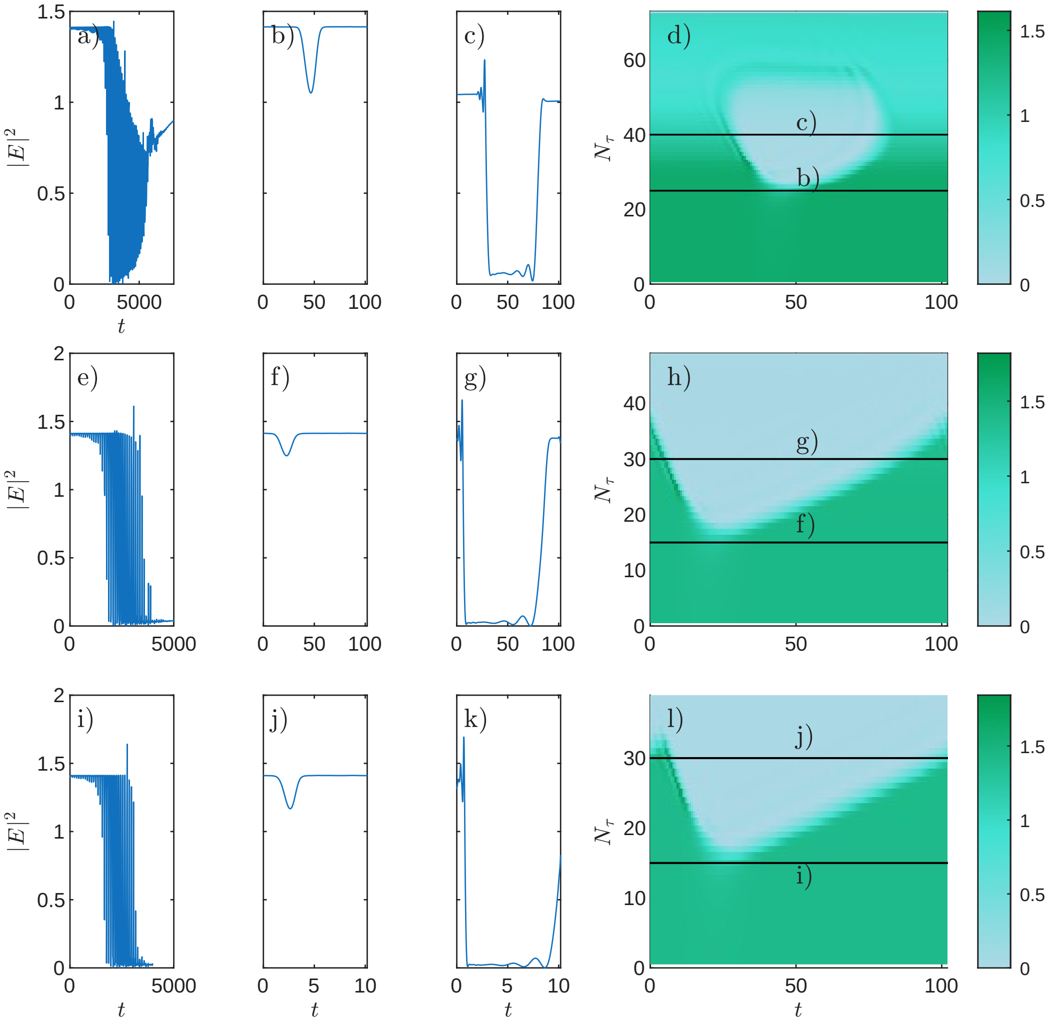

Figure 24: Interaction stages of the dark excitable pulses for $\gamma = 10^{-5}$, 10^{-4}, and 10^{-3}. d), h), l) $|E|^2$ intensity during phases of length τ from the start to the end of the interaction stage. b), c), f), g), j), k) Different phase profiles corresponding to the interaction stages in a), e), i).

In contrast to the bright solutions, the interaction dynamics in this parameter regime allow the trajectory to settle exclusively at E_-. Consequently, only a single type of dark excitable pulse exists. The different stages of the interaction process are illustrated in Figure 24.

For $\gamma = 10^{-4}$ and $\gamma = 10^{-5}$, the thermal time scale is sufficiently slow such that the interaction completes at E_{-} before the trajectory reaches the first fold point. In contrast to that, for $\gamma = 10^{-3}$, the interaction terminates on the upper nullcline after the fold point has been crossed.

Unlike the bright excitable states, the interaction phases of the dark excitable pulses originate from a single pulse without tail oscillations. Small-amplitude tail oscillations emerge only after the full connection to E_{-} has formed. However, their amplitude is too small to enable interaction with other pulse tails. Therefore, no phase shift of the pulse fronts is observed.

10 Summary and outlook

This thesis has investigated the nonlinear dynamics and noise-driven excitability of the thermal Kerr–Gires–Tournois interferometer (KGTI), a microresonator with Kerr nonlinearity, thermal detuning, and delayed optical feedback. The analysis was structured around two complementary limits: the non-delayed slow-fast ODE system and the full delay differential equation (DDE).

Non-delayed system. In the singular limit of vanishing external-cavity round-trip time, the system reduces to a three-dimensional ODE with a clear separation between fast field dynamics and slow thermal evolution. The critical manifold $\mathcal{S}$, defined by the nullcline of the intracavity field, was derived analytically and shown to consist of two stable branches connected by an unstable repelling branch, with fold points marking the transitions between them. As the thermal coefficient μ_α is varied, the continuous-wave (CW) fixed point undergoes a supercritical Hopf bifurcation, and the resulting small-amplitude limit cycle grows rapidly into a large-amplitude relaxation oscillation through a Canard explosion. The sequence of bifurcations connecting the Hopf bifurcation to the canard explosion involves multiple fold and period-doubling bifurcations, and ultimately gives rise to several Feigenbaum cascades resulting in deterministic chaos. The maximum Lyapunov exponent was computed numerically and shown to be consistent with the logarithm of the maximal Floquet multiplier along the period-doubling branches for one selected Feigenbaum structure. Noise-driven excitability was identified at the stable CW fixed point prior to the Canard explosion, where Gaussian white noise can push the orbit beyond the fold point and induce isolated relaxation pulses. Coherence resonance was demonstrated at the stable fixed point on the onset of the second Hopf bifurcation at the upper fold point.

Delayed system. Including the external-cavity delay τ introduces an entirely new class of solutions: delay-induced switched states. These τ-periodic solutions correspond to delay-induced switched states that connect the two stable branches of the critical manifold, and persist beyond the first Hopf bifurcation of the CW branch but reconnect in a subcritical Hopf bifrucation at the second Hopf point, which also serves as a bifurcation point for the supercritical Hopf bifurcation of the relaxation oscillations. An analytical approximation for the effectively frozen δ_c of these solutions was derived via a balance condition. The branch structure in the bifurcation diagram, including higher-order switched states with multiple intra-period pulses, was calculated numerically for different values of the thermal time scale γ.
Also, two distinct noise-driven excitability regimes were characterized in the delayed system. *Bright excitability* arises near the lower fold point when a canard bifurcation

is present ($\gamma \ll \tau^{-1}$). Noise-induced pulses undergo an interaction stage governed by the delayed feedback, producing at least three distinct pulse types with different periods determined by the switched-state dynamics. The type distribution depends sensitively on the noise amplitude. *Dark excitability* arises near the upper fold point and is observed across all investigated timescale ratios. A single pulse type is found, and coherence resonance is recovered. In both regimes for the lower fold point (delayed and non-delayed), the inter-excitation time is phase-locked to the underlying periodic attractor, generating mixed-mode oscillations that are absent in the deterministic system.

In summary, the thermal KGTI system unifies slow-fast dynamics, Canard transitions, delay-induced multistability, stochastic excitability and timescale competition with pulse interaction within an optical microcavity, making it an interesting model system for nonlinear optics.

Outlook. In future work, a more detailed investigation of the mechanisms underlying the switched states and the associated bifurcation would be highly valuable. In particular, a refined path-variational ansatz could be developed to provide a more accurate description of the positioning of the invariant cycle. Furthermore, the interaction between the pulses warrants a more systematic analysis, especially with regard to the relationship between pulse intensity and mutual proximity, as well as the relevant interaction timescales, which have so far only been characterized heuristically. Further parameters that alter the feedback strength like the coupling h or feedback mirror reflectivity η are likely to change the interaction stages and could in principle be of interest. Moreover, a more detailed investigation of many pulse switched states for even slower timescales and their bifurcation scenarios possibly in two parameter path continuations including the thermal timescale can be of interest.

References

[1] Eugene M. Izhikevich. *Dynamical Systems in Neuroscience: The Geometry of Excitability and Bursting*. Illustrated edition. Cambridge, MA: MIT Press, 2007, p. 441. ISBN: 9780262090438.

[2] Richard FitzHugh. “Impulses and Physiological States in Theoretical Models of Nerve Membrane”. In: *Biophysical Journal* 1.6 (1961), pp. 445–466. ISSN: 0006-3495. DOI: `https://doi.org/10.1016/S0006-3495(61)86902-6`.

[3] J. Zagora et al. “Excitability in chemical and biochemical pH-autocatalytic systems”. In: *Faraday Discuss.* 120 (0 2002), pp. 313–324. DOI: `10.1039/B103534G`.

[4] Elias R. Koch et al. “Thermo-optical dynamics in injected Kerr micro-cavities with strong time-delayed feedback”. In: *Chaos, Solitons & Fractals* 202 (2026), p. 117595. ISSN: 0960-0779. DOI: `https://doi.org/10.1016/j.chaos.2025.117595`.

[5] J. Nagumo, S. Arimoto, and S. Yoshizawa. “An Active Pulse Transmission Line Simulating Nerve Axon”. In: *Proceedings of the IRE* 50.10 (1962), pp. 2061–2070. DOI: `10.1109/JRPROC.1962.288235`.

[6] B. Lindner et al. “Effects of noise in excitable systems”. In: *Physics Reports* 392.6 (2004), pp. 321–424. ISSN: 0370-1573. DOI: `https://doi.org/10.1016/j.physrep.2003.10.015`.

[7] Arkady S. Pikovsky and Jürgen Kurths. “Coherence Resonance in a Noise-Driven Excitable System”. In: *Physical Review Letters* 78.5 (1997), pp. 775–778. DOI: `10.1103/PhysRevLett.78.775`.

[8] Luca Gammaitoni et al. “Stochastic resonance”. In: *Rev. Mod. Phys.* 70 (1 Jan. 1998), pp. 223–287. DOI: `10.1103/RevModPhys.70.223`.

[9] Jan Sieber et al. *DDE-BIFTOOL Manual - Bifurcation analysis of delay differential equations*. 2016. arXiv: `1406.7144 [math.DS]`. URL: `https://arxiv.org/abs/1406.7144`.

[10] Steven H. Strogatz. *Nonlinear Dynamics and Chaos*. Boca Raton, Florida: CRC Press, 2015, pp. 309–354. ISBN: 978-0-8133-4910-7.

[11] A. L. Hodgkin and A. F. Huxley. “A quantitative description of membrane current and its application to conduction and excitation in nerve”. In: *The Journal of Physiology* 117.4 (1952), pp. 500–544. DOI: `https://doi.org/10.1113/jphysiol.1952.sp004764`.

[12] A. L. Hodgkin. “Evidence for electrical transmission in nerve”. In: *The Journal of Physiology* 90.2 (1937), pp. 183–210. DOI: `https://doi.org/10.1113/jphysiol.1937.sp003507`.

[13] Bard Ermentrout. “Type I Membranes, Phase Resetting Curves, and Synchrony”. In: *Neural Computation* 8.5 (July 1996), pp. 979–1001. ISSN: 0899-7667. DOI: 10.1162/neco.1996.8.5.979.

[14] M. Krupa and P. Szmolyan. “Extending Geometric Singular Perturbation Theory to Nonhyperbolic Points—Fold and Canard Points in Two Dimensions”. In: *SIAM Journal on Mathematical Analysis* 33.2 (2001), pp. 286–314. DOI: 10.1137/S0036141099360919.

[15] Thomas G. Seidel, Julien Javaloyes, and Svetlana V. Gurevich. “A normal form for frequency combs and localized states in Kerr–Gires–Tournois interferometers”. In: *Opt. Lett.* 47.12 (June 2022), pp. 2979–2982. DOI: 10.1364/OL.457777.

[16] Elias R. Koch. “Square-waves and pulsating dynamics in time-delayed active micro-cavities”. Master’s thesis. Münster: Universität Münster, Jan. 2023.

[17] U. Thiele. *Lecture "Introduction to Numerical Continuation"*. Version 1. Feb. 2021. DOI: 10.5281/zenodo.4544848.

[18] Marzena Ciszak et al. “Intermittent chaotic spiking in the van der PolNagumo system with inertia”. In: *Chaos, Solitons & Fractals* 167 (2023), p. 113053. ISSN: 0960-0779. DOI: https://doi.org/10.1016/j.chaos.2022.113053.

[19] Stefan Ruschel and Serhiy Yanchuk. “Delay-induced switched states in a slow–fast system”. In: *Philosophical Transactions of the Royal Society A: Mathematical, Physical and Engineering Sciences* 377.2153 (July 2019), p. 20180118. ISSN: 1364-503X. DOI: 10.1098/rsta.2018.0118.

[20] Y. Chembo Kouomou et al. “Chaotic Breathers in Delayed Electro-Optical Systems”. In: *Phys. Rev. Lett.* 95 (20 Nov. 2005), p. 203903. DOI: 10.1103/PhysRevLett.95.203903.

Eigenständigkeitserklärung

Hiermit versichere ich, dass die vorliegende Arbeit über
Thermally induced excitability in injected microcavities with time-delayed feedback

selbstständig von mir und ohne fremde Hilfe verfasst worden ist, dass keine anderen Quellen und Hilfsmittel als die angegebenen benutzt worden sind und dass die Stellen der Arbeit, die anderen Werken – auch elektronischen Medien – dem Wortlaut oder Sinn nach entnommen wurden, auf jeden Fall unter Angabe der Quelle als Entlehnung kenntlich gemacht worden sind. Mir ist bekannt, dass es sich bei einem Plagiat um eine Täuschung handelt, die gemäß der Prüfungsordnung sanktioniert werden kann.

Ich erkläre hiermit, dass ich Kenntnis von einer zum Zweck der Plagiatskontrolle vorzunehmenden Speicherung der Arbeit in einer Datenbank sowie von ihrem Abgleich mit anderen Texten zwecks Auffindung von Übereinstimmungen habe.

Ich versichere, dass ich die vorliegende Arbeit oder Teile daraus nicht anderweitig als Prüfungsarbeit eingereicht habe.

18.04.26 Aaron Schumacher

(Datum, Unterschrift)